ANNUAL REVIEWS

Annual Review of Earth and Planetary Sciences

Physics of Melt Extraction from the Mantle: Speed and Style

Richard F. Katz,[1] David W. Rees Jones,[2] John F. Rudge,[3] and Tobias Keller[4,5]

[1]Department of Earth Sciences, University of Oxford, Oxford, United Kingdom; email: richard.katz@earth.ox.ac.uk

[2]School of Mathematics and Statistics, University of St Andrews, St Andrews, United Kingdom

[3]Department of Earth Sciences, University of Cambridge, Cambridge, United Kingdom

[4]School of Geographical and Earth Sciences, University of Glasgow, Glasgow, United Kingdom

[5]Institute of Geochemistry and Petrology, ETH Zürich, Zürich, Switzerland

Annu. Rev. Earth Planet. Sci. 2022. 50:507–40

First published as a Review in Advance on February 25, 2022

The *Annual Review of Earth and Planetary Sciences* is online at earth.annualreviews.org

https://doi.org/10.1146/annurev-earth-032320-083704

Keywords

magma, asthenosphere, rheology, partial melting, channelization, dunite, rock microstructure, mid-ocean ridge, subduction, mantle heterogeneity

Abstract

Melt extraction from the partially molten mantle is among the fundamental processes shaping the solid Earth today and over geological time. A diversity of properties and mechanisms contribute to the physics of melt extraction. We review progress of the past ~25 years of research in this area, with a focus on understanding the speed and style of buoyancy-driven melt extraction. Observations of U-series disequilibria in young lavas and the surge of deglacial volcanism in Iceland suggest this speed is rapid compared to that predicted by the null hypothesis of diffuse porous flow. The discrepancy indicates that the style of extraction is channelized. We discuss how channelization is sensitive to mechanical and thermochemical properties and feedbacks, and to asthenospheric heterogeneity. We review the grain-scale physics that underpins these properties and hence determines the physical behavior at much larger scales. We then discuss how the speed of melt extraction is crucial to predicting the magmatic response to glacial and sea-level variations. Finally, we assess the frontier of current research and identify areas where significant advances are expected over the next 25 years. In particular, we highlight the coupling of melt extraction with more realistic models of mantle thermochemistry and rheological properties. This coupling will be crucial in understanding complex settings such as subduction zones.

- Mantle melt extraction shapes Earth today and over geological time.
- Observations, lab experiments, and theory indicate that melt ascends through the mantle at speeds ~30 m/year by reactively channelized porous flow.
- Variations in sea level and glacial ice loading can cause significant changes in melt supply to submarine and subaerial volcanoes.
- Fluid-driven fracture is important in the lithosphere and, perhaps, in the mantle wedge of subduction zones, but remains a challenge to model.

1. INTRODUCTION

Melting occurs when the internal energy of a crystalline solid is sufficient to break lattice bonds, creating disorder at the molecular scale. The melt therefore has higher entropy and higher enthalpy than its solid residue; it typically also has a different equilibrium composition. These differences confer a lower viscosity and, in general, a distinct density. In the presence of a gravitational potential, melt segregates from its residue if a permeable pathway is available. That segregation, which occurs at the grain scale, transports heat and chemistry over much larger scales. Indeed, melt segregation creates planetary radial structure, creates and destroys chemical heterogeneity, cools the interior, and shapes the surface and atmosphere.

On Earth, these processes are manifest in close association with plate tectonics and mantle convection. Indeed, magmatism is generally discussed in terms that are specific to a tectonic context (e.g., spreading centers, subduction zones, and intraplate hotspot volcanoes). The presence of primitive basaltic volcanism in each of these settings provides clear evidence that at least some of the magma is derived from mantle melting. For each tectonic context, there are a variety of geographical instances where observations are made. These data raise questions that pertain to both local characteristics and global systematics. A question general enough to apply to all settings and to physics from the scale of grains to that of tectonic plates is, What are the speed and style of melt extraction from where it is produced in the asthenosphere mantle to where it interacts with the lithosphere? The present review is organized around this question and investigates the physical processes it evokes.

Asthenosphere: the hot, approximately adiabatic, upper mantle just beneath the lithosphere

Lithosphere: the conductively cooled, outermost region of the solid Earth, above the asthenosphere

Porosity: the volume fraction of melt in a control volume that contains many grains and pores; equivalent to the melt fraction

The simplest null hypothesis for the style of melt transport is diffuse porous flow. This states that melt produced at the grain scale is transported through a permeable network of melt tubules (pores) along the junctions between grains. It also states that porosity is diffuse, i.e., that it varies slowly in space and time. In this context, the gravitational body force, acting on the density difference between solid and liquid, $\Delta\rho = \rho_s - \rho_\ell$ (typically positive), drives segregation. A balance between this buoyancy force and the viscous drag force associated with Darcian porous flow leads to a characteristic melt speed (sometimes called the percolation velocity) of

$$w_0 = \frac{k\Delta\rho g}{\phi\mu}, \qquad 1.$$

where ϕ is porosity, g is the magnitude of gravitational acceleration, μ is the viscosity of the liquid, and k is the permeability, a function of the grain size and porosity discussed below. A typical value of w_0 for conditions of partially molten regions of the upper mantle is probably in the range of 0.01–1 m/year. Constraints on melt speed discussed below, however, indicate speeds in the range 1–100 m/year. Here and in previous work, this difference has been attributed to a style of flow that is channelized, rather than diffuse. The present review is mostly concerned with the causes and consequences of flow localization into channels.

The poro-viscous continuum theory underlying our discussion of partially molten rock was published by McKenzie (1984) (see also Fowler 1984). Its broad physical basis and key applications were reviewed by Stevenson & Scott (1991); Kohlstedt & Zimmerman (1996) discussed the physics with a focus on rheological properties. A recent book, *The Dynamics of Partially Molten Rock* (Katz 2022), provides a comprehensive and didactic treatment, including a history of its development and abundant references. And while the percolation velocity was noted by earlier researchers, McKenzie (1984) recognized a natural length scale of magma–mantle interaction. This compaction length, discussed in Section 2.3, is closely related to the dimensions of emergent flow localization, porosity waves, and boundary layers.

Our focus in this review is on the physical mechanisms that account for the discrepancy in melt-transport speed between diffuse porous flow and observational constraints. We build on the landmark review by Kelemen et al. (1997) and trace forward some of the themes identified there. Within the limited space of this review, we mostly discuss and cite literature published after the review by Kelemen et al. (1997); the reader should consult that and other publications cited here for references to earlier works. In Section 2, we review physics at the grain and laboratory scales that underpins continuum theories at larger scales. We highlight experiments that demonstrate the link between reactive melting and channelized melt flow. In Section 3, we review two observational constraints on magma speed. We then discuss a family of physics-based models of channelized flow. In Section 3.3, we discuss the hypothesis that sea level (SL) modulates submarine magmatism. In Section 4, we scan the horizon of current research to identify themes and ideas that may form the basis of discoveries in the next 25 years. We conclude with a summary and list of future issues to motivate further research.

2. PHYSICS OF MELT EXTRACTION IN THE LABORATORY

Mantle partial melting is dispersed at the grain scale, where juxtaposition of different minerals leads to eutectic-like solidus lowering. In the absence of significant deviatoric stress, the solid–liquid microstructure that forms is controlled by surface energy. The system tends to a state of textural equilibrium, where the energy bound up in solid–liquid and solid–solid interfaces is minimized. For mantle rocks, the low surface energy of the solid–liquid interface stabilizes an interconnected pore network distributed between grains.

How rapidly is textural equilibrium established? In laboratory experiments, textural equilibrium is reached in a matter of hours, but such experiments have much finer grain sizes than the mantle. If the rate of textural equilibration of a pore is limited by diffusion within the melt phase, then the equilibration time τ is expected to scale as the cube of pore size L, $\tau = L^3/K$, with a prefactor K that depends on temperature. For a typical mantle grain size $d \sim 3$ mm and a porosity of $\phi \sim 0.1\%$, the pore size is $L = d\sqrt{\phi} \sim 100$ μm. An empirical value of $K \sim 10^{-21}$ m^3 s^{-1} (Holness & Siklos 2000) yields an equilibration time $\tau \sim 30$ years.

Liquid–solid interaction at the grain scale ($\leq$ mm) has consequences at the continuum scale ($\geq$ m to km). Laboratory experiments provide a means to measure and understand the physics of this interaction and a basis for deriving constitutive laws to be used in continuum models. This section reviews laboratory experiments and how the relevant physics has been quantitatively upscaled.

2.1. Permeability

The key material property for understanding melt migration is the permeability of the partially molten rock. This depends on the size d of the mineral grains, the porosity ϕ of the rock, and, importantly, how the melt is arranged at the grain scale (i.e., on the microstructure). Typically

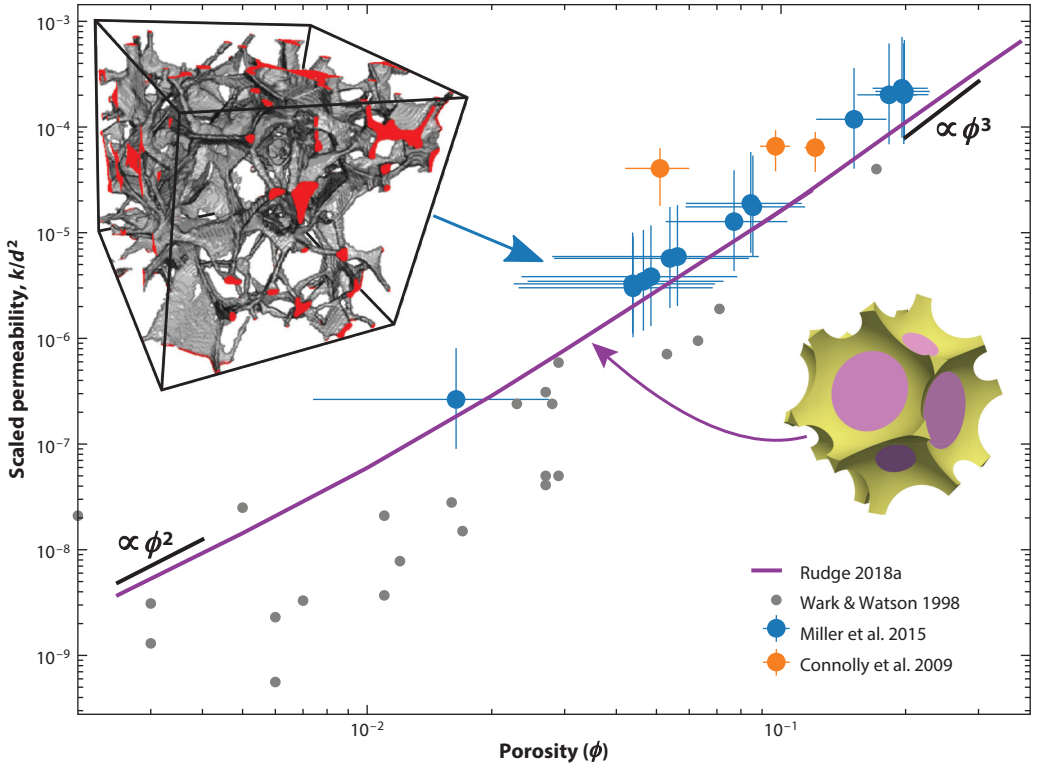

Figure 1

Scaled permeability (permeability k divided by the square of grain size d) plotted against porosity ϕ for a selection of experimental and theoretical studies. The textural-equilibrium model of identical truncated octahedral grains with a dihedral angle of 40° is shown (*purple curve*), adapted from Rudge (2018a). The geometry is illustrated in the bottom right with melt network in yellow and grain in pink, with a porosity of 5%. Also shown are rock-analog experimental measurements on synthetic quartzites (*gray dots*), adapted from Wark & Watson (1998). Flow calculations of permeability are shown (*blue dots*) using the measured pore space of olivine + basalt samples, adapted from Miller et al. (2015). The top left shows a microtomography image for a porosity of 5%, adapted with permission from Miller et al. (2014). The scaled permeability plotted assumes an average grain size of 35^{+25}_{-15} μm for all experiments (similar to those quoted in Miller et al. 2014). High-pressure, high-temperature centrifuge experiments on olivine + basalt samples by Connolly et al. (2009) are shown (*orange dots*). Finally, the slopes on this plot for $k \propto d^2\phi^2$ and $k \propto d^2\phi^3$ (*black lines*) are shown. For porosity less than 2%, the model textural-equilibrium permeability can be well approximated by $k = d^2\phi^2/1{,}600$ (von Bargen & Waff 1986, Rudge 2018a); for porosity greater than 10%, it can be well approximated by $k = d^2\phi^3/75$.

permeability is described by a semiempirical law of the form $k = d^2\phi^n/C$, where n is an exponent between 2 and 3, and C is a numerical prefactor encapsulating effects of pore geometry.

Different approaches have been taken to estimate permeability, and some recent estimates are shown in **Figure 1**. One approach is to assume a particular geometry for the melt network and then calculate the permeability by solving a Stokes flow problem for melt flow at the pore scale. Rudge (2018a) presented an example of this approach, where a textural-equilibrium geometry for a collection of identical, truncated, octahedral grains is assumed (**Figure 1**). At small porosity, the melt forms a connected network of tubes along the grain edges and the permeability scales as $k \propto d^2\phi^2$. As porosity increases, more of the grain faces become wetted and the permeability transitions to scaling as $k \propto d^2\phi^3$.

The textural-equilibrium geometry model by Rudge (2018a), shown in **Figure 1**, is highly idealized and does not account for the heterogeneity of grain size and type seen in real rocks.

To quantify the effect of heterogeneity in grain size, Miller et al. (2014, 2015) recently estimated the permeabilities of olivine + basalt samples by microtomographic imaging of the pore space (**Figure 1**), followed by Stokes flow calculation of permeability. Their results are broadly consistent with the idealized, theoretical estimates. Miller et al. (2016) further explored the effect of heterogeneity in grain type by imaging olivine + orthopyroxene (opx) + basalt samples. The presence of opx may act to reduce permeability because the dihedral angle of an opx–opx–melt triple junction is ∼70°, much larger than the ∼40° typical for an olivine–olivine–melt junction. Dihedral angles greater than 60° are associated with a threshold porosity above which pores form a permeable network (von Bargen & Waff 1986, Rudge 2018a) and below which there is zero permeability. In the heterogeneous olivine + opx + basalt samples examined by Miller et al. (2016), however, no significant differences in permeability from the olivine + basalt samples were seen, even with 40% opx present. One should bear in mind that the permeabilites quoted by Miller et al. (2016) are limited by resolution to porosities greater than 3%, and the influence of opx on permeability at smaller porosities is thus unclear.

There have been several experimental efforts to directly measure the permeability of rock samples by measuring the rate of fluid flow in response to an applied pressure gradient. **Figure 1** includes experimental results by Wark & Watson (1998), who studied synthetic quartzite as a rock analog, and Connolly et al. (2009), who studied olivine + basalt samples. These experiments are broadly in line with the simple textural-equilibrium models, although the estimates by Connolly et al. (2009) are somewhat higher and those by Wark & Watson (1998) are somewhat lower.

2.2. Viscosity

Crucial to any geodynamic model of melt extraction by viscous processes is an understanding of how the skeleton of solid mineral grains resists deformation. This resistance is described by two viscosities: a shear viscosity η and a compaction viscosity ζ. The shear viscosity relates the deviatoric stress and deviatoric strain rate, just as for a pure solid material. The compaction viscosity is a two-phase flow concept and describes resistance to the closing (compaction) or opening (decompaction) of pore space due to a difference in pressure between the solid and the melt.

Figure 2 plots estimates of the compaction and shear viscosity as a function of porosity ϕ for both micromechanical models and laboratory experiments. One of the simplest micromechanical models, adopted by many authors (e.g., Scott & Stevenson 1986; Sleep 1988; Bercovici et al. 2001; Hewitt & Fowler 2008; Simpson et al. 2010a,b; Schmeling et al. 2012), is to assume the skeleton of grains acts like a uniform viscous fluid with shear viscosity η_s. For small porosity, these models imply $\eta \sim \eta_s(1-\phi)$ and $\zeta \sim D\eta_s/\phi$, where D is an $O(1)$ geometrical prefactor. However, a uniform viscous-fluid model fails to capture the true physics at the grain scale, which involves the motion of lattice defects, and sliding, precipitation, and diffusion along grain boundaries (Kohlstedt & Hansen 2015). Such grain-scale physics can be upscaled to produce continuua with a macroscale viscous rheology; the resulting compaction and shear viscosities as a function of porosity are quite different from models that assume a grain-scale viscous rheology. **Figure 2** shows model viscosities for Coble creep [grain-boundary diffusion creep, similar to the models of Cooper & Kohlstedt (1984, 1986) and Takei & Holtzman (2009a)] and Nabarro-Herring creep (diffusion through the grain volume). Diffusion-creep models predict a more rapid decrease in the shear viscosity with porosity than uniform viscous-fluid models but a more modest variation in compaction viscosity. For small porosity, the Nabarro-Herring creep models have a weak (logarithmic) singularity in compaction viscosity, and Coble creep models have a compaction viscosity that is 5/3 times the shear viscosity (Takei & Holtzman 2009a, Rudge 2018b).

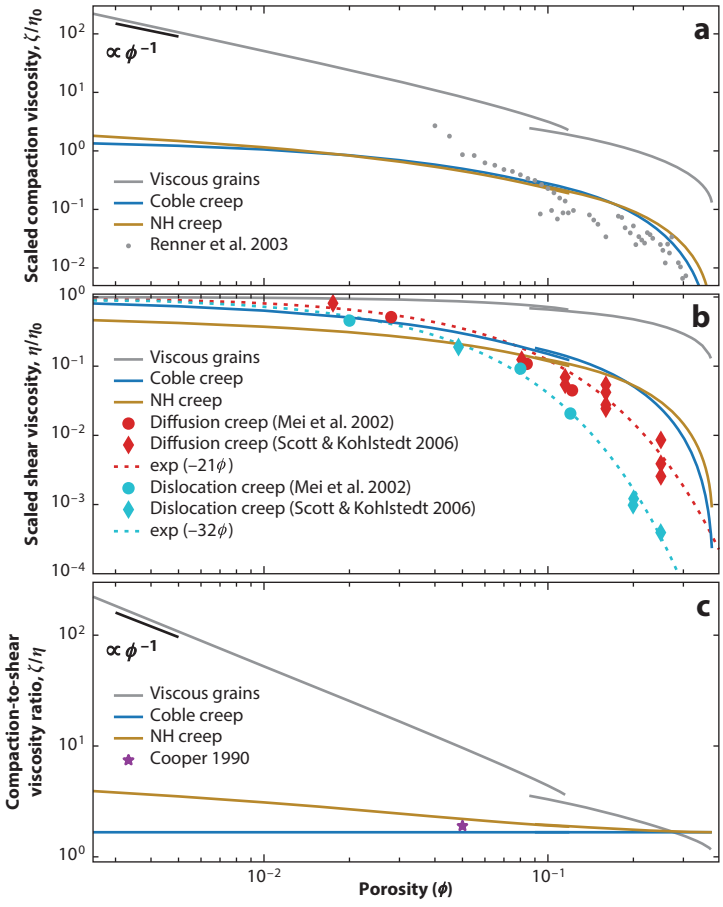

Figure 2

Models and experimental data on the viscosities of partially molten rocks as a function of porosity. (*a*) The compaction (also known as bulk) viscosity ζ, scaled by η_0, the shear viscosity at zero porosity. (*b*) The shear viscosity η scaled by η_0. (*c*) The ratio of compaction viscosity to shear viscosity. In each panel, three model curves are plotted as solid lines. Each model has the same melt geometry but different grain-scale physics. The geometry assumes textural equilibrium for truncated octahedral grains with a dihedral angle of 40°, as illustrated in **Figure 1**. A break in the curves occurs around 10% porosity due to a topological transition where some of the grain faces become wetted. The curves labeled viscous grains assume the matrix of solid grains acts as a uniform viscous fluid, where the interior of each grain is deforming. The other curves are based on grain-scale models of diffusion creep (Rudge 2018b), where grains are rigid and relative motion is by plating or removal of matter at grain boundaries. For compaction viscosity, the C-423 and C-479 (olivine + Li-silicate melt) data of Renner et al. (2003) are shown, scaled assuming $\eta_0 = 2 \times 10^{13}$ Pa s. Different choices of η_0 move data up and down on the plot, but do not change the relative positions of the points. For shear viscosity, the compilation of data on dry, synthetic peridotites by Scott & Kohlstedt (2006) is shown, along with data on olivine + basalt deformed under hydrous condition by Mei et al. (2002). Dotted lines show the exponential-law fits, proposed by Kelemen et al. (1997), to the Scott & Kohlstedt (2006) data, $\eta = \eta_0 \exp(-\alpha\phi)$, where $\alpha = 21$ for diffusion creep and $\alpha = 32$ for dislocation creep. Mei et al. (2002) suggested slightly different fit parameters (not shown), with $\alpha = 26$ for diffusion creep and $\alpha = 31$ for dislocation creep. Panel *c* shows a single estimate of the compaction/sheer viscosity ratio from a four-point bending experiment by Cooper (1990). Abbreviation: NH, Nabarro-Herring.

Laboratory experiments have been performed to estimate the shear viscosity of partially molten rock, but few have attempted to estimate the compaction viscosity (notable exceptions are Cooper 1990 and Renner et al. 2003). The experimental studies on shear viscosity (e.g., Scott & Kohlstedt 2006, Mei et al. 2002; **Figure 2**) indicate a more rapid drop-off in the shear viscosity with increasing porosity than the diffusion-creep models predict; this may be due to effects not captured by an idealized melt geometry, e.g., anisotropic surface energies that cause wetting of grain boundaries at smaller porosity. It should be noted that the experimental data in **Figure 2** are limited to relatively high porosity ($\phi \gtrsim 1\%$), higher than typical mantle porosity [$\phi \sim 0.1\%$ (McKenzie 2000)].

The rheological behavior of partially molten rock at very small porosity ($0 \leq \phi < 0.01\%$) is poorly understood. In this case, additional physical processes need to be taken into account. For example, the models shown in **Figure 2** assume an infinite diffusivity in the melt phase, whereas at sufficiently small porosity, the finite diffusivity of the melt can be the rate-limiting control on the shear viscosity (Takei & Holtzman 2009b). It has been suggested, both theoretically (Takei & Holtzman 2009a) and experimentally (Faul & Jackson 2007, McCarthy & Takei 2011), that very small fractions of melt can lead to a drop in the shear viscosity from melt-free values by a factor of 5 or more. The theoretical argument of Takei & Holtzman (2009a) is based on the notion that very small amounts of melt can act as a significant fast path for diffusion. Subsequent calculations have predicted a more modest weakening due to this effect (Rudge 2018b). Moreover, recent studies have suggested that much of the weakening seen in experiments might be attributable to subsolidus phenomena, such as the development of premelting films on grain boundaries as the solidus temperature is approached from below (Yamauchi & Takei 2016, Takei 2017).

A major shortcoming of most existing models of upscaled physical properties such as permeability or viscosity is that they assume a fixed microstructure. When a partially molten rock is deformed, its microstructure can change substantially, and this can have a significant effect on macroscale properties. For example, Takei (2005) observed significant additional wetting of grain boundaries in rock-analog samples placed under shear, with corresponding changes in their elastic, anelastic, and viscous properties. Moreover, grain size is not a fixed quantity but evolves in time [e.g., grain growth (Breithaupt et al. 2021)] and with deformation [e.g., dynamic recrystallization (Austin & Evans 2007)]. Models that capture the evolution of microstructure during deformation are in their infancy, but there have been some notable developments. In particular, Takei & Holtzman (2009c) showed how an anisotropic microstructure leads to an anisotropic effective viscosity for Coble creep. Such an anisotropic viscosity couples shear and compaction deformation, and can explain laboratory experiments on partially molten rocks deformed in torsion that show radial segregation of melt (Qi et al. 2015). Bercovici & Ricard (2012) introduced a continuum, two-phase flow formalism with evolution equations for average properties of the microstructure such as grain size and interface curvature, but we do not yet have models that capture a time-evolving anisotropic fabric.

2.3. The Compaction Length

Viscously deformable porous media have a natural length scale δ, the compaction length, which is defined as (McKenzie 1984)

$$\delta = \sqrt{\frac{k}{\mu}\left(\zeta + \tfrac{4}{3}\eta\right)}. \qquad 2.$$

The compaction length sets the scale over which compaction occurs when there is an obstruction to flow. It controls the thickness of boundary layers and the spacing of localization features. It depends on the melt viscosity μ, as well as the permeability k, the shear viscosity η, and

the compaction viscosity ζ, whose dependence on the grain-scale physics was discussed in the previous subsections.

While there is still much uncertainty in the appropriate values for the parameters in Equation 2, it is possible to make order-of-magnitude estimates for typical compaction lengths in the mantle beneath ridges (Kelemen et al. 1997). Taking a typical shear viscosity $\eta \sim 5 \times 10^{19}$ Pa s, a typical compaction viscosity $\zeta = \frac{5}{3}\eta$, a typical melt viscosity $\mu \sim 10$ Pa s, a porosity–permeability relation $k = d^2\phi^2/1{,}600$, and a grain size $d = 3$ mm, we have $\delta \sim 300$ m for a porosity $\phi = 0.1\%$, and $\delta \sim 3$ km for a porosity $\phi = 1\%$. However, if compaction viscosity was significantly greater than shear viscosity, then the estimates of compaction length would be correspondingly larger. For example, at a porosity of $\phi = 0.1\%$, $\zeta = 550\eta$ for the viscous grain models of **Figure 2**, leading to $\delta \sim 4$ km; and for a porosity of $\phi = 1\%$, $\zeta = 51\eta$, and thus $\delta \sim 12$ km.

2.4. Reactive Melting and Channelization in the Laboratory

As magma moves from higher to lower pressure, its shifting equilibrium chemistry drives incongruent melting reactions (Kelemen 1990, Longhi 2002). The pressure variation within the mantle is dominantly vertical, although nonvertical gradients also occur due to dynamical effects. The decrease in pressure as magma rises leads it to become undersaturated in silica. Silica-undersaturated magma in turn reacts with the mantle rock, dissolving pyroxene and precipitating olivine (harzburgite → dunite). This dissolution reaction leads to a net transfer of mass from the rock to the magma phase, and so this process is sometimes called reactive melting (Kelemen 1990). Dunite channels found in ophiolites (**Figure 3*c***) are interpreted as the geological remnant of this process (Kelemen et al. 1992, Braun & Kelemen 2002), suggesting that melt flow was focused in the regions that became the dunites rather than being distributed uniformly.

Laboratory experiments help us to understand the physical and chemical controls that lead to channelized flow. The large-scale solubility gradient driving reaction in the mantle is impossible to realize in the laboratory. Instead, a similar chemical reaction is created by placing a melt reservoir that is undersaturated in silica, an alkali basalt, next to a partially molten rock formed from a mixture of olivine and pyroxene (**Figure 3*a***). This creates a sharp jump in undersaturation, in contrast to the gradual gradient in the mantle (**Figure 3*d***). Infiltration of melt from the reservoir into the partially molten rock drives the same type of chemical melting reaction that occurs in the mantle.

However, the mere existence of undersaturation is insufficient to cause reactive channelization. Experiments by Morgan & Liang (2003) without forced melt flow produced reactive dissolution in a fringe between the melt source and the partially molten rock; the thickness was controlled by chemical diffusion. They observed no marked channelization (**Figure 3*e***).

Rather, sufficiently rapid melt flow is required for reactive channelization. Pec et al. (2015, 2017) also conducted contact-style experiments at conditions similar to the mantle. They applied a pressure gradient to drive melt from the reservoir into the partially molten rock, without significantly affecting the equilibrium chemistry. In experiments where the pressure gradient, and hence the melt velocity, was high enough, the reactive front localized into reactive channels (**Figure 3*f***). Pec et al. (2020) extended these experiments by considering several types of partially molten rock (werhlite, harzburgite, lherzolite). They showed that the critical conditions for channelization varied with the type of rock. While werhlite and harzburgite samples had tube-shaped channels (**Figure 3*b***), one lherzolite sample had a vein-shaped channel. The latter was tentatively attributed to a fracture-like phenomenon.

Dunite channels found in ophiolites have a tabular morphology (Kelemen et al. 1992, 2000; Braun & Kelemen 2002), which contrasts with the tube-shaped channels found experimentally.

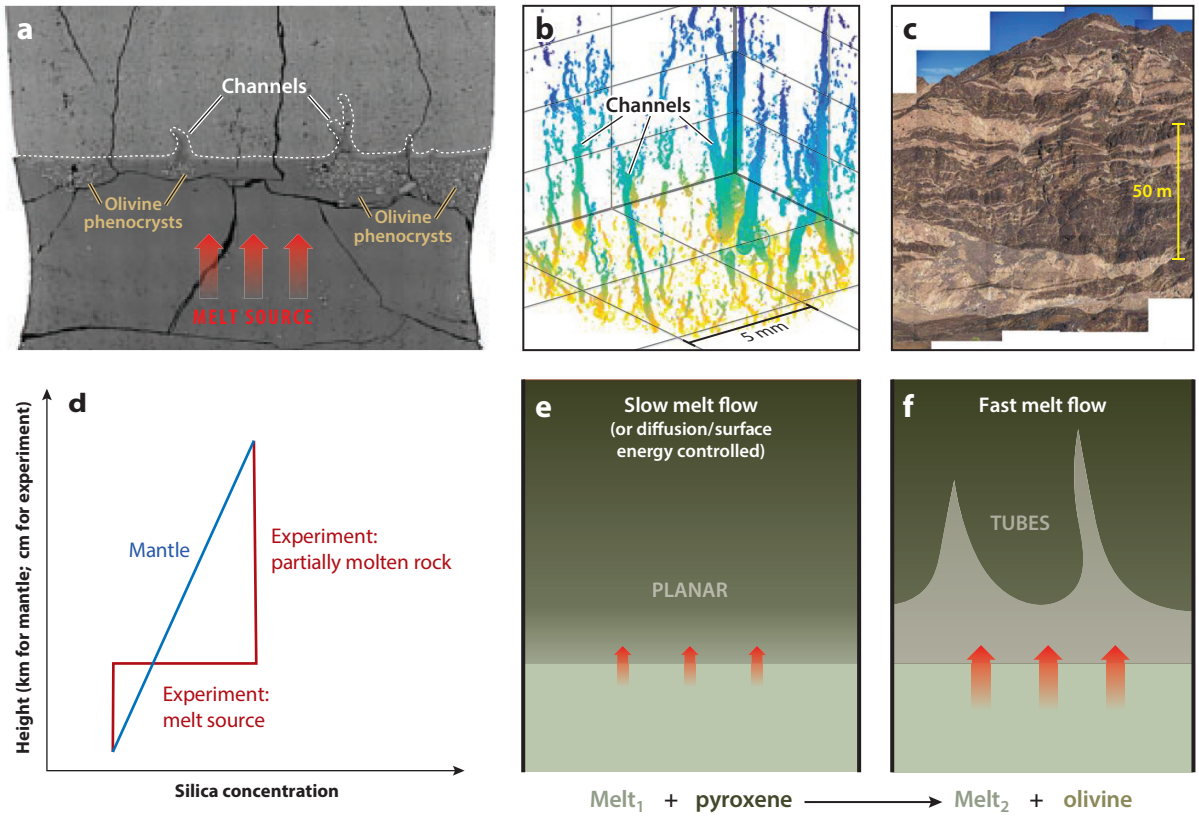

Figure 3

(*a*) Experiments where melt is driven into a partially molten rock causing channels to form. Panel *a* adapted with permission from Pec et al. (2017). (*b*) Computed tomography scan showing that the channels are tube shaped. Panel *b* adapted with permission from Pec et al. (2020). (*c*) Field observations of tabular dunites from the Muscat Massif ophiolite. Panel *c* adapted with permission from Braun & Kelemen (2002). The paleogravity direction is perpendicular to the present exposure such that the dunites would have been near vertical at the time of formation. The dunite channels are the lighter-colored features embedded in the darker harzburgite. (*d*) Schematic diagram of reaction channelization. Silica concentration varies gradually with depth in the mantle and has a stepwise jump in the experiments between an undersaturated melt reservoir and the partially molten rock sample. (*e*) For slow melt flow, there is a near-planar reaction front. (*f*) For fast melt flow, tube-shaped reactive channels emerge.

More broadly, although the chemistry of the reaction in the experiments is similar to that in the mantle, the fluid dynamical aspects (that are crucial to the instability) are different between the settings. Therefore, modeling has a significant role in interpreting these laboratory experiments in terms of melt extraction from the mantle, a question we turn to in Section 3.2.1. Moreover, the experiments showed that microphysical properties of the partially molten rock control whether channelization occurs. These properties must therefore be characterized both at the laboratory scale and at the tectonic scale.

3. PHYSICS OF MELT EXTRACTION IN THE ASTHENOSPHERE

Asthenospheric melt transport operates on timescales, over pressure gradients, and at strain rates that will never be accessible in laboratory experiments. These scales also make the natural setting inaccessible to direct observation; measurement of proxies for the quantities of interest

is usually the best we can do. Physics-based models are then required to interpret the proxy data, and this complicates the testing of process hypotheses against data. Ultimately, however, it is the quantitative consistency between laboratory physics, observations of nature, and theoretical models that gives confidence in a physical understanding of the natural system. In this section we review constraints derived from observations and models based on our understanding of the physics.

3.1. Observational Constraints on Magma Speed

Constraints on the speed of magma transport are indirect and scarce. Here we review two that are widely recognized as valid (if not unambiguous) measures.

3.1.1. Uranium series. Important constraints on the speed of melt transport through the mantle come from observations of uranium-series (U-series) disequilibria in lavas. The basic premise in using U series to provide minimum bounds on ascent speeds is simple, but there are many subtleties in practice. Before the mantle melts, it is in a state of radioactive equilibrium where each intermediate isotope in a decay chain is produced at approximately the same rate as it decays. On melting, some elements more readily enter the melt than others, causing the decay chain to be out of equilibrium in the melt. Isotopes in the chain return to radioactive equilibrium on a timescale set by their half-life. If radioactive disequilibrium is seen at the surface, it means that the transport process must have taken place within a few half-lives of the isotope in question.

The subtleties arise in identifying the particular physical process that causes the disequilibria and depth at which that process takes place. For example, fractionation can occur throughout the depth of the melting region if melt interacts chemically with the matrix as it migrates (e.g., the equilibrium porous flow model in Spiegelman & Elliott 1993). ^{226}Ra excesses may be affected by diffusion within plagioclase in magma chambers (Van Orman et al. 2006). Some isotopes in the decay chains (e.g., ^{210}Pb) have volatile intermediate isotopes that might be affected by near-surface degassing (Turner et al. 2012). Attributing a near-surface signal to a deep, mantle-melting cause will lead to a vast overestimation of melt ascent rates. A more robust constraint comes from the observed excesses of ^{230}Th to ^{238}U in mid-ocean ridge (MOR) basalts. The half-life of ^{230}Th is 75,000 years. Th is thought to be more incompatible than U only in the presence of garnet. If the source rock is lherzolite, garnet is present only beneath the garnet–spinel transition at ∼80 km depth. The observed ^{230}Th excesses then constrain the melt ascent rate to be at least 1 m/year. If the observed excesses in the shorter-lived isotopes ^{231}Pa and ^{226}Ra also originate at such depths, melt transport speeds through the mantle may be 100 m/year or higher (Stracke et al. 2006, Turner et al. 2001). If the ^{210}Pb disequilibria originate at depth, melt transport would be inferred to be even faster, with transport speeds up to 1 km/year (Rubin et al. 2005).

Interpretation of U series is further complicated by the likely lithological heterogeneity of the mantle. The presence of garnet pyroxenite allows for garnet signatures of fractionation to be produced at shallower depths (Elkins et al. 2019). For a more detailed discussion of U-series constraints on melt ascent, see Elliott & Spiegelman (2003) and Turner & Bourdon (2011).

3.1.2. Icelandic eruption chronology. More direct constraints on melt-transport speeds come from observations of the magmatic response to deglaciation in Iceland, particularly during the most recent major deglaciation around 12,000 years ago. Eruption rates surged by a factor of 30 or more following the deglaciation. The most natural explanation for this surge is that unloading of the ice caused mantle rock at depth to rapidly decompress, increasing melting rates and leading to an increase in eruption rates following the transport of the melt to the surface (Jull & McKenzie

1996). The observed time lag between glacial unloading and the surge in eruption rates yields an estimate of the melt-transport timescale (Maclennan et al. 2002).

Chemical observations of lavas erupted during and following the periods of deglaciation provide additional information. Notably, lavas erupted during the surge are depleted in rare earth elements (REEs) by up to 70% (Maclennan et al. 2002, Sinton et al. 2005, Eason et al. 2015). Modeling by Eksinchol et al. (2019) has indicated that the chemistry of the erupted lavas is strongly affected by melt-transport speeds, as melts produced at shallow depths are depleted in REEs and are transported to the surface faster than the REE-enriched melts that are produced deeper. Field observations can identify lavas erupted under ice, and the modeling shows that the amount of subglacial volcanism is also sensitive to melt-transport speeds: More rapid rates of melt ascent lead to a greater fraction of lavas erupting under ice. Eksinchol et al. (2019) concluded that the Icelandic observations are best explained by average rates of melt transport through the mantle of ~100 m/year.

However, rates of melt transport estimated during Iceland's recent deglaciation may not be representative of the rates of melt transport during typical MOR melting. Iceland is underlain by a hot mantle plume that causes a significant increase in melting rates compared with that expected for pure passive upwelling; this is reflected in the thick (~20 km) crust beneath much of the island. Furthermore, the melting rates following deglaciation are an order of magnitude greater than the background, steady-state melting rates. Rees Jones & Rudge (2020) used a 1D melting column model to quantify how unrepresentative the deglaciation estimates are and concluded that while typical transport rates may be lower than the Icelandic estimates, average melt-transport speeds of at least 10 m/year should be seen across the global ridge system.

Implications of the U-series and deglaciation-volcanism constraints on magma speed are discussed in the sidebar titled Implications of Observational Constraints on Melt Extraction.

IMPLICATIONS OF OBSERVATIONAL CONSTRAINTS ON MELT EXTRACTION

The speed of melt transport, as inferred from the two constraints discussed in Section 3.1, is too large to be consistent with the null hypothesis of diffuse porous flow (Equation 1). To see this, consider a column of mantle upwelling directly beneath the ridge axis. The vertical melt flux is proportional to the degree of melting and the upwelling rate, $\phi w_0 = FW_0$. By combining this expression with Equation 1 and the porosity–permeability relation $k = d^2\phi^2/1{,}600$ from **Figure 1**, we find the estimates

$$w_0 = d\left(\frac{\Delta\rho g}{1600\mu}FW_0\right)^{1/2}, \qquad \phi = \frac{1}{d}\left(\frac{1600\mu}{\Delta\rho g}FW_0\right)^{1/2}.$$

On this basis, a grain size of 6 cm corresponds to a melt velocity of about 30 m/year and a porosity of 0.1%, while a grain size of 3 mm corresponds to a melt velocity of 1.5 m/year and a porosity of 2%. (Calculations were made with representative parameter values $\Delta\rho = 500$ kg/m^3, $g = 10$ m/s^2, $\mu = 10$ Pa s, $F = 0.25$, and $W_0 = 0.1$ m/year.) Inferences of melt velocity are thus connected to inferences about porosity, and both are controlled by the permeability law. For diffuse porous flow to meet the constraints on melt speed requires a grain size that is much larger than observed in xenoliths.

An alternative hypothesis is transport through dikes in the solid asthenosphere; this mechanism is observed to occur in the lithosphere (Rivalta et al. 2015). While diking cannot be entirely ruled out on physical grounds, there is no evidence that it is common in the asthenosphere (though see Python & Ceuleneer 2003 and Section 4.2). There is good evidence, reviewed by Kelemen et al. (1997), for the hypothesis of porous flow localized into high-flux channels. We review the physics behind this in Section 3.2.

3.2. Mechanisms of Flow Channelization

We next review mechanisms of magmatic localization into channels. We provide some background but focus on ideas published since this subject was reviewed by Kelemen et al. (1997).

Compaction rate $\mathcal{C}$: divergence of the solid velocity; $\mathcal{C}$ is negative for a medium that is compacting

Sensitivity of compaction viscosity: slope of the relationship $\zeta(\phi)$, which can be characterized by the dimensionless quantity

$$m = -\left.\frac{\mathrm{d}\zeta}{\mathrm{d}\phi}\right|_{\phi_0} \frac{\phi_0}{\zeta_0},$$

which generalizes the exponent in the scaling $\zeta \propto \phi^{-m}$

3.2.1. Reactive flow instabilities. Is the reaction infiltration instability a viable mechanism for channelization in the mantle (Aharonov et al. 1995, Kelemen et al. 1995)? To form, channels must grow fast enough compared to the upwelling rate of the mantle. Stability analysis allows us to estimate the linear growth rate σ_{react} of channels (Aharonov et al. 1995, Hesse et al. 2011, Rees Jones & Katz 2018). Three properties control σ_{react}:

1. The potential for reactive melting b (units m^{-1}). This can be thought of as the ratio of the change in the equilibrium concentration of silica in the magma per unit depth divided by the degree of supersaturation of silica in reactive melts.
2. The speed of background melt flow before the onset of channels w_0 (units m year^{-1}). Throughout this subsection, we use a subscript $_0$ to denote a steady-state, unchannelized flow.
3. The sensitivity of permeability to porosity, as expressed by the permeability exponent n (no units). See Section 2.1.

Extra reactive melting caused by extra melt flow increases the porosity. This positively feeds back on the permeability and hence the melt velocity. Given these properties, a simple first estimate of the maximum growth rate (which we refine below) is

$$\sigma_{\mathrm{react}} = nbw_0. \qquad 3.$$

This comes from estimating the extra melt flux per unit extra porosity as nw_0, which is then multiplied by b to obtain the extra melting. The estimates $n = 2$, $b = 2 \times 10^{-6}$ m^{-1}, and $w_0 = 1$ m year^{-1} give $\sigma_{\mathrm{react}} = 4 \times 10^{-6}$ year^{-1}, or a growth timescale (time in which channel porosity changes by a factor of $e = 2.7$) of $1/\sigma_{\mathrm{react}} = 0.25$ Myr. This is significantly less than the upwelling time for a parcel of partially molten mantle to rise across the melting region (about 1 Myr for an upwelling rate of 10 cm/year or 10 Myr for an upwelling rate of 1 cm/year).

The length scale at which channels emerge is highly uncertain, depending on both a length scale for chemical equilibration and the compaction length (Aharonov et al. 1995, Spiegelman et al. 2001). Rees Jones & Katz (2018) obtained estimates both when the system is effectively rigid and when the system is subject to strong compaction (for further details, see the **Supplemental Text**).

Supplemental Material >

Compaction can also stabilize the system when the compaction viscosity decreases rapidly with increasing porosity. A linear estimate of the (negative) contribution to the growth rate by this mechanism is

$$\sigma_{\mathrm{compact}} = \frac{-\mathcal{C}_0}{\zeta_0 + \frac{4}{3}\eta_0} \left.\frac{\mathrm{d}\zeta}{\mathrm{d}\phi}\right|_{\phi_0}, \qquad 4.$$

where the background compaction rate is $\mathcal{C}_0 < 0$ and the slope is $\mathrm{d}\zeta/\mathrm{d}\phi < 0$ (**Figure 2*a***). For further details, including a derivation, see the **Supplemental Text**. A negative contribution to the total growth rate proportional to the slope of $\zeta(\phi)$ was first reported by Hesse et al. (2011). Significant differences between studies arise from choices of $\zeta(\phi)$. Thus, if $\zeta \propto \phi^{-1}$, compaction can completely stabilize the linear system, as shown by Hewitt (2010). However, if the sensitivity of compaction viscosity is much smaller, the reactive instability can win out, as shown by Aharonov et al. (1995), who used a constant compaction viscosity (zero slope). The diffusion-creep models shown in **Figure 2*a*** have an intermediate sensitivity. Similarly, Hesse et al. (2011) found that

compaction–dissolution waves (a generalization of the concept of a reactive channel in which the growth rate has an imaginary part, leading to wavelike behavior) would be expected in mantle conditions for weak sensitivity but not for strong sensitivity. Evidently, understanding rheological properties is crucial.

Linear analysis applies only to the initial development of channels. What happens when channels grow beyond the linear regime? Two-dimensional numerical simulations by Spiegelman et al. (2001) suggest a channel spacing consistent with the predictions of the linear theory. In such nonlinear solutions, dynamic pressure gradients can create dynamic solubility gradients and promote the coalescence of channels. However, Rees Jones et al. (2021) argued that such pressure gradients at MORs are typically much smaller than the vertical lithostatic pressure gradient.

The width of the channels, once they develop, is considerably smaller than the spacing and appears to be dominantly controlled by diffusion within the parameter regime explored by Spiegelman et al. (2001). As discussed above, the effective diffusive length scale approaches zero as $R \to \infty$, so calculations based on chemical equilibrium localize to the grid scale (Hewitt 2010). The total flux of melt is dominated by the flow through channels, so arguably the inferences about melt velocity discussed previously should be interpreted as relating to melt velocity in the channels.

Liang et al. (2010) and Schiemenz et al. (2011) performed high-resolution numerical calculations with boundary conditions that favored the formation of a single channel and explored lithological features of channel formation. **Figure 4** shows an example of the nonlinear evolution of a reactive channel. As the soluble component of the mantle is exhausted within the center of the channel, the high-porosity region splits into two, with flow focused on the margins of the dunite. If this picture is correct, it challenges the idea that the dunites themselves are the pathways of channelized flow, which has important geochemical consequences (Liang et al. 2010). Strong compaction occurs in the center of the channel in these calculations, which were performed with compaction-viscosity sensitivity $\zeta \propto \phi^{-1}$; this behavior is likely to depend on the sensitivity. It is possible that an increase in grain size within the channel, as suggested by field observations (Hansen & Warren 2015) and experiments (Morgan & Liang 2005), might counteract the tendency for channels to split. Likewise, the reduction in pyroxene content would increase permeability in the channel due to the effect of pyroxene on permeability (Zhu & Hirth 2003, Miller et al. 2016), although these ideas remain largely unexplored.

A further way that mantle chemistry might affect reactive channelization is the presence of volatile species. Keller & Katz (2016) and Keller et al. (2017) showed that reactive channelization is enhanced by the presence of volatiles, particularly around the onset depth of dry melting. This is because this depth region has both a significant gradient in the equilibrium volatile content in the melt and an increasing upward melt flux. This idea could be analyzed in greater detail. Volatiles might be especially important in driving deep channelization, which appears to be necessary to match geochemical and geophysical observations (Jull et al. 2002, Liu & Liang 2019).

At a MOR, channels are formed in a more complex environment than a simple upwelling column. The prevalent direction of melt flow will include a component toward the ridge axis (for a review, see Sim et al. 2020), leading to reactive channels that also bend toward the ridge axis (Keller et al. 2017). However, the mantle shear flow driven by plate spreading has a rotational component. This acts to rotate channels that form near vertically such that they tend to point away from the ridge axis (Baltzell et al. 2015, Keller et al. 2017). At the same time, shearing a porosity-weakening material can generate an independent mechanism of melt localization. We discuss this further in Section 3.2.3.

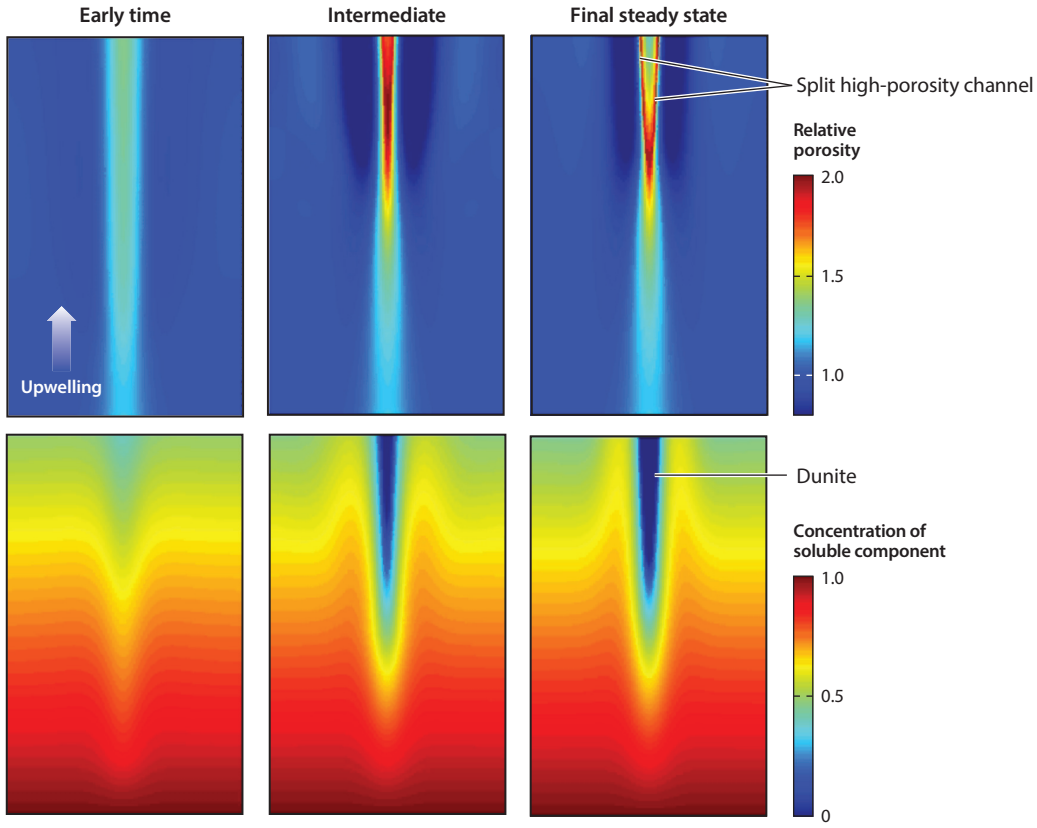

Figure 4

Nonlinear evolution of reactive channels. The top row shows the relative porosity. The bottom row shows the concentration of the soluble component, which is progressively exhausted within the central channel. See Liang et al. (2010) and Schiemenz et al. (2011). Figure adapted with permission from the supplementary movie of Schiemenz et al. (2011).

3.2.2. Lithological heterogeneity. The models considered above analyze the emergence of channels from infinitesimal perturbations to the steady background state of diffuse porous flow. It is well established, however, that the mantle is heterogeneous in lithology, major-element chemistry, and hence fusibility at a broad range of scales. In this context, it may be invalid to analyze the system in terms of a steady background state with small perturbations. Instead, the heterogeneity should be regarded as a leading-order feature of the mantle. Does this finite perturbation introduce a propensity for channelization (Lundstrom et al. 2000), and does that propensity overcome stabilizing factors such as a porosity dependence of compaction viscosity? The relationship between heterogeneity and channelization depends on the coupling between thermochemistry and dynamics under melt segregation. This coupling remains poorly understood.

Investigations to date have been heavily weighted toward either the petrologic or the geodynamic perspective. The former have focused on the chemistry of eclogite- and pyroxenite-derived melts (Hirschmann & Stolper 1996; Pertermann & Hirschmann 2003a,b; Kogiso et al. 2004b; Kogiso & Hirschmann 2006) and their interaction with the ambient peridotite (Kogiso et al. 2004a). At pressures greater than 2 GPa, this interaction depends on the source composition of the pyroxenite in relation to a thermal divide in its melting behavior. Pyroxenites more

Si rich than the thermal divide (including eclogites) produce quartz-normative melts at an invariant point; these melts crystallize when they infiltrate peridotite. Pyroxenites on the mafic side of the divide produce Si-undersaturated (nepheline-normative) melts; these react with peridotite to give a net increase in the liquid fraction. Only the latter can immediately trigger a channelization feedback. More modest heterogeneity in source composition, such as spatial variations of pyroxene fraction in lherzolite, could also nucleate and organize the structure of channels.

Geodynamic perspectives have largely ignored the subtleties of the petrology associated with mantle heterogeneity to focus on the physics of magmatism. Schiemenz et al. (2011) represented heterogeneity as a persistent, localized, excess melt influx on the isochemical boundary of a canonical reactive-melting model (**Figure 4**). To go beyond this, a model must incorporate some representation of variability in bulk composition. A straightforward approach uses a two-component thermochemical system, representing fertile and refractory end members in solid solution, where the solidus and liquidus temperatures increase with concentration of the refractory component. **Figure 5** shows snapshots from numerical simulations using this two-component system. **Figure 5*a–c*** is from a tectonic-scale model of a MOR with distributed heterogeneity (Katz & Weatherley 2012), whereas **Figure 5*d–g*** shows an upwelling column with an isolated, initially circular, fertile enclave (Weatherley & Katz 2012). Melting preferentially occurs in fertile regions, in both the more-fusible heterogeneities and the channels that transport their melt. Equilibrium according to the phase diagram fixes their temperature lower than the surrounding refractory regions. Heat from those surroundings diffuses inward, further enhancing melting while suppressing it in the refractory regions (Sleep 1984, Katz & Rudge 2011). This leads to a key difference from canonical models of reactive flow (Section 3.2.1): that in the mantle adjacent to channels the porosity is (or approaches) zero. The high-permeability channel is thus contained within a low-permeability jacket. **Figure 5*d*** shows that melt speed in the channels is enhanced relative to diffuse porous flow.

Weatherley & Katz (2012) quantified the coupling between (two-component) petrology, thermodynamics, and flow. They did so in the context of a linearized phase diagram, as in **Figure 5*b***, with solidus temperature that increases with refractory concentration at slope M and a constant difference ΔC in solid–liquid composition. In this case, the volumetric melting rate can be decomposed as

$$\Gamma = \Gamma_W + \Gamma_R + \Gamma_T, \qquad 5.$$

where Γ_W represents decompression melting and Γ_R represents reactive melting. The final term, $\Gamma_T = \mathcal{G}\kappa\nabla^2 T \approx \mathcal{G}\kappa M\nabla^2 C_\ell$, represents melting driven by thermal diffusion (chemical diffusion is negligibly slow). The symbol κ is the thermal diffusivity; the prefactor $\mathcal{G}$ is defined in the margin.

The contribution from each of these terms is shown as a fraction of Γ in **Figure 5*e–g***. The symbol C_ℓ denotes the refractory-component concentration in the liquid, which is related to equilibrium temperature via the phase diagram (**Figure 5*b***). Hence, a vertical channel carrying fertile melt will have $\Gamma_T \propto \partial^2 C_\ell/\partial x^2 > 0$. A comparison of the contributions of Γ_R and Γ_T indicates that, for the case of a heterogeneity with a significant solidus difference from the ambient mantle, the melting powered by thermal diffusion plays a larger role than that by chemical reaction.

Jordan & Hesse (2015) showed that two-component, solid-solution petrology can also capture the case of melts from a heterogeneity that reactively crystallizes to create an impermeable shell. As discussed above, this behavior is expected for quartz-normative pyroxenite enclaves. Lundstrom et al. (2000) argued that the products of this reactive crystallization would, at lower pressure, be preferentially melted and drive channelization. However, it remains unclear if/how the behavior predicted in the context of highly simplified petrology (Katz & Weatherley 2012, Weatherley &

Prefactor $\mathcal{G}$: thermal cost of melting, units K^{-1};

$$\mathcal{G} = \frac{1}{L/c_P + M\Delta C},$$

where L is latent heat and c_P is specific heat capacity

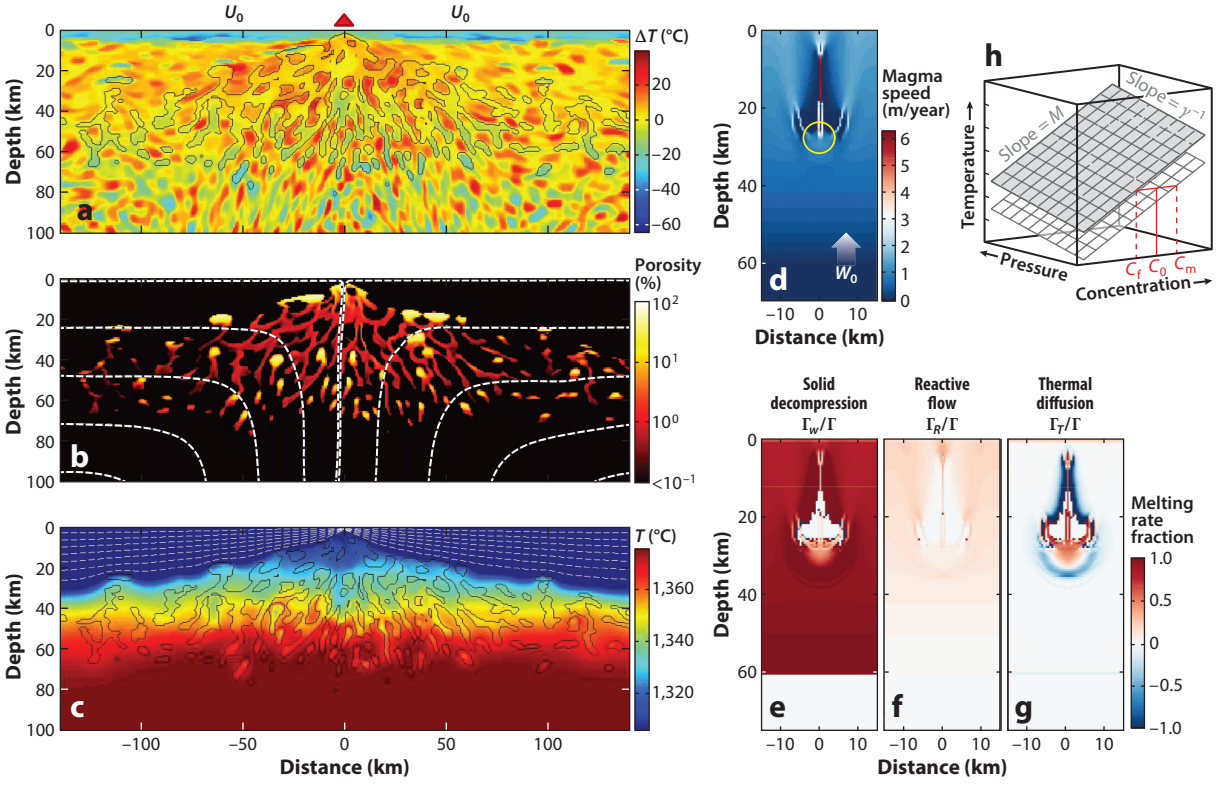

Figure 5

Melting and melt transport in a heterogeneous mantle. Heterogeneity is represented in terms of a two-component, equilibrium thermochemical system with full solid solution. Panels *a–c* show a snapshot from a MOR simulation with half-spreading rate U_0. (*a*) The solidus-temperature differences (color scale in °C) from a reference value due to chemical heterogeneity. The solid black contours outline the partially molten regions. The heterogeneity field, prior to modification by flow or melting, is generated by filtering a random field to remove wavelengths less than 5 km and rescaling to the desired range of solidus temperature. (*b*) The porosity (%; *colors*) and streamlines of the solid mantle (*white dashed curves*). (*c*) Potential temperature (°C). The color scale is truncated to highlight temperature variations associated with melting of fertile enclaves, which remain cooler than ambient. Black contours are as in panel *a*. Panels *a–c* adapted with permission from Katz & Weatherley (2012). Panels *d–h* show a snapshot of a 2D column with a circular, fertile enclave upwelling at $W_0 = 4$ cm/year. The initial solidus of the enclave is 30°C lower than the ambient mantle at any pressure. (*d*) Magma speed. The yellow circle outlines where the enclave would be if there were zero melting. (*e–g*) Contributions to the melting rate arising from solid decompression, reactive flow, and thermal diffusion, respectively, as fractions of the total melting rate (see Equation 5 and text following). (*h*) The linearized phase diagram used to represent petrology in the MOR and upwelling column models. A constant compositional difference ΔC separates the solidus and liquidus surfaces, which have constant slopes M and γ^{-1} in refractory concentration and pressure, respectively. Panels *d–h* adapted with permission from Weatherley & Katz (2012). Abbreviation: MOR, mid-ocean ridge.

Katz 2012, Jordan & Hesse 2015, Keller & Katz 2016) is consistent with more realistic petrological models and, indeed, with the natural system.

Melt-transport models of MORs have also illustrated how segregation can create heterogeneity. In simulations by Ghods & Arkani-Hamed (2000), Katz (2008), and Keller et al. (2017), melt produced in the wings of the melting region ascends to, pools at, and ultimately solidifies into the base of the lithosphere. This metasomatism creates chemical heterogeneity in the lithosphere (Pilet et al. 2008, Rochat et al. 2017). If the melt that crystallizes at the lithosphere–asthenosphere boundary (LAB) is itself derived from a heterogeneous mantle, a recursive petrological process

could lead to extreme chemical variability. Alternatively, the dominant pattern of heterogeneity may be simple enough to approximate using a combination of lherzolite, harzburgite, and pyroxenite, in which case inversion methods may constrain their proportions (e.g., Ito & Mahoney 2005, Shorttle et al. 2014). But refractory lithologies, by definition, contribute little to melt production and are therefore difficult to detect (Stracke 2021). Moreover, melt extraction can both create (Spiegelman & Kelemen 2003) and destroy (Bo et al. 2018) geochemical variability, making it difficult to disentangle the effects of source and transport.

3.2.3. Shear-driven melt bands. Laboratory experiments in which a partially molten rock is subjected to shear show melt aligned in sheets (bands in the cross section, as we refer to them below) where the porosity is higher than average (Holtzman et al. 2003, Kohlstedt & Holtzman 2009). If the melt bands found in laboratory experiments occur beneath MORs, they would have a significant impact on melt migration. Bands give rise to an anisotropic permeability, with melt preferentially flowing toward or away from the ridge axis depending on their orientation. Katz et al. (2006) showed that a strongly strain rate–weakening and porosity-weakening shear viscosity gives rise to bands that have an instantaneous growth rate with an alignment that would focus melt toward the ridge axis, potentially explaining the narrowness of the volcanic zone. Melt bands may have further implications for interpretation of geophysical data, but here our focus is on melt migration.

Do melt bands grow fast enough in the mantle to matter? Is this growth robust in spite of other physical mechanisms that might alter or destroy them? What alignment is preferred, and how sensitive is this to the degree of strain rate weakening, which is generally considered smaller than assumed by Katz et al. (2006)? How do melt bands interact with reactive channels and, if both form, which are more important?

A series of studies have addressed these questions. For a sense of how fast melt bands grow, we first discuss their linear growth rate σ_{shear}. Three properties control σ_{shear}:

1. The solid strain rate $\dot{\gamma}_0$ (units s^{-1}),
2. The sensitivity of shear viscosity to porosity, and
3. The compaction-to-shear viscosity ratio in the background state.

Given these properties, a simple first estimate of the maximum growth rate, which occurs when extension is oriented across bands, is

$$\sigma_{\text{shear}} = -\frac{2\dot{\gamma}_0}{\zeta_0 + \frac{4}{3}\eta_0} \left.\frac{\mathrm{d}\eta}{\mathrm{d}\phi}\right|_{\phi_0}. \qquad 6.$$

This linear estimate (Stevenson 1989), based on a Newtonian rheology, comes from balancing the shear stress associated with viscosity variation across bands with compaction stress. Growth is somewhat faster for a strain rate–weakening (Katz et al. 2006, Butler 2009) or anisotropic viscosity (Takei & Katz 2015), but Equation 6 is still a good rough estimate, albeit with a different dependence on the angle of porosity bands. Takei & Holtzman (2009c) and Butler (2012) showed that anisotropic diffusion-creep viscosity leads to low-angled bands. Two-phase damage may also be a viable mechanism for this (Rudge & Bercovici 2015, Butler 2017). In all models, pressure variation means that growth is suppressed at wavelengths comparable to or greater than the compaction length. (For further details, see Rees Jones et al. 2021.)

Buoyancy-driven flow is negligible in the laboratory but significant in the mantle. Butler (2009, 2012) showed that buoyancy-driven flow does not significantly alter the growth of bands but can affect the direction of melt flow.

A further complication is that MOR spreading does not drive a pure-shear mantle flow. Rather, the mantle flow consists of both a shearing part (that drives band formation) and a rotational part

(that rotates the bands as they form). This is potentially significant because bands can be rotated away from orientations in which they grow, to those in which they decay—so analyses based on the instantaneous growth rate such as by Katz et al. (2006) are probably not a reliable guide to the preferred alignment of bands. Gebhardt & Butler (2016) extended the methodology of Spiegelman (2003) to account for advection and rotation of a small-scale parcel of porosity bands by the mantle corner flow. The idea is to express the porosity as the sum of a background state ϕ_0 (which varies gradually over the depth of the melting region) and a set of porosity bands with wavenumber $\boldsymbol{k}(t)$ and log-amplitude $s(t)$: $\phi = \phi_0 + \exp[i\boldsymbol{k}(t) \cdot \boldsymbol{x} + s(t)]$. The wavevector and amplitude evolve along streamlines of the solid flow accounting for advection, rotation, and growth in amplitude, as shown in **Figure 6*a***. Gebhardt & Butler (2016) showed that bands that initially point toward the ridge axis are rotated such that they instead focus melt toward the base of the lithosphere.

However, reactive channels typically form with a near-vertical alignment, so what happens when both reactive channels and melt bands can form? Rees Jones et al. (2021) accounted for both shear- and reaction-driven growth. Shear also affects the growth of reactive channels, particularly through the preferred morphology of channels. The ratio of instantaneous shear to reactive growth is controlled by the ratio $\sigma_{\text{shear}}/\sigma_{\text{react}}$, plotted in **Figure 6*b***. In the absence of shear, reactive channels form with cylindrical shape. Embedded in an extensional shear flow, reactive channels

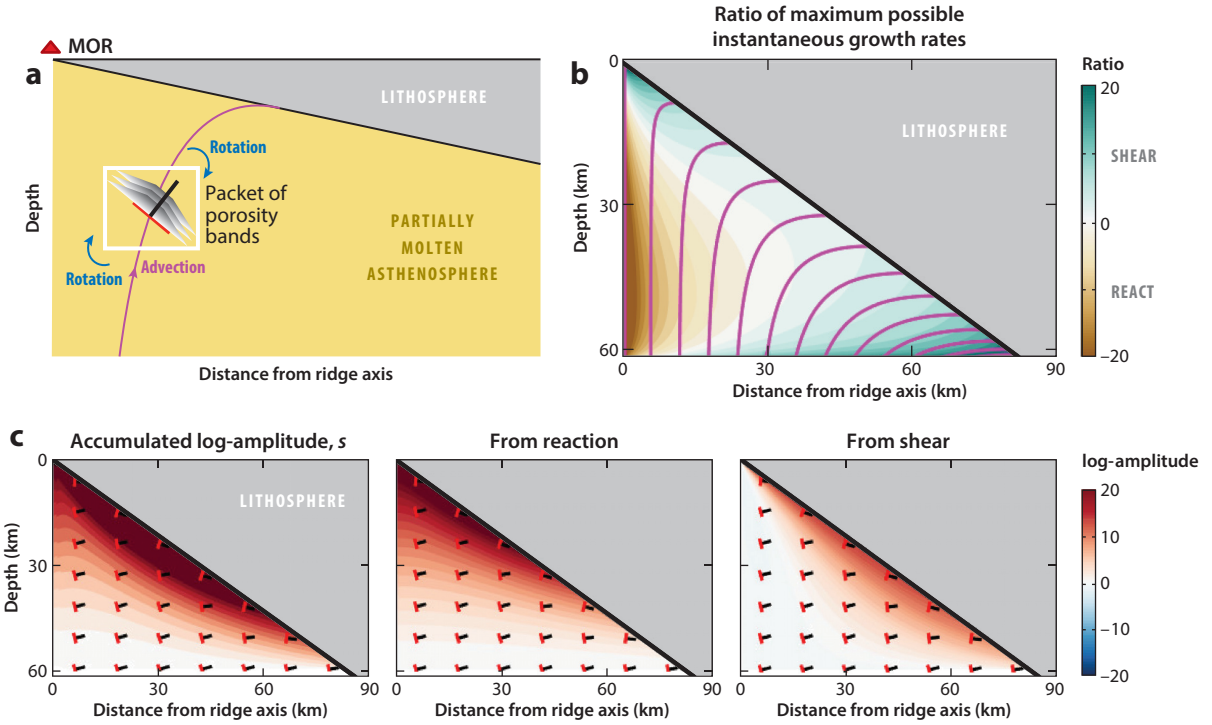

Figure 6

Melt channel and band emergence in a MOR corner flow. (*a*) Sketch of a MOR with a packet of melt bands that evolves along streamline of solid flow. (*b*) Ratio of the maximum possible instantaneous growth rates of shear-driven to reaction-driven melt bands. In practice, shear-driven bands are typically oriented such that the actual growth rate is smaller than the maximum. (*c*) log-amplitude of porosity bands where the total is split into reactive and shear contributions. Black line segments show the orientation of the wavevector, and red line segments show the corresponding porosity bands, which are perpendicular to the wavevector, as marked on panel *a*. Abbreviation: MOR, mid-ocean ridge. Figure adapted from Rees Jones et al. (2021).

form as tabular bodies, the orientation of which is vertical when $\sigma_{react} \gg \sigma_{shear}$ and controlled by shear when $\sigma_{shear} \gg \sigma_{react}$. Rees Jones et al. (2021) showed that reaction dominates shear over most of the MOR system, except near the base of the lithosphere (**Figure 6*c***). Channels form deep within the mantle, favoring a subvertical orientation that is then rotated away from the ridge axis. Thus, reactive infiltration in the presence of shear is an important mechanism of deep channelization that explains the observed tabular dunites and the disequilibrium between erupted lavas and the upper mantle. Shear may also affect melt migration near the base of the lithosphere, but it probably does not contribute to focusing melt toward the ridge axis.

Magmatic solitary wave: isolated excess of porosity that propagates, due to liquid buoyancy, with constant speed and shape; a well-studied feature of poro-viscous magma dynamics

3.2.4. Decompaction weakening and failure. Could channelized melt flow occur by a purely mechanical process? Connolly & Podladchikov (1998, 2007) proposed a rheological model that incorporates material yielding in response to liquid overpressure. They hypothesized that the compaction viscosity ζ (Section 2.2) is 10^2–10^3 times smaller for decompaction as for compaction. In other words, the compaction viscosity depends on the sign of the pressure difference between liquid and solid, such that opening pores induces less viscous resistance than closing them. By incorporating this into the canonical theory for partially molten rocks, they showed how it causes magmatic solitary waves to elongate and become gravity-aligned channels.

At the leading edge of a solitary wave, magma buoyancy gives the liquid an overpressure ($P_\ell > P_s$) that causes decompaction, while at the trailing edge it gives a liquid underpressure ($P_\ell < P_s$) that causes compaction. If the compaction viscosity ζ is independent of the sign of the pressure difference (as typically assumed) and the background state is uniform, then the porosity wave is symmetrical across a plane through its maximum and normal to gravity. In contrast, when the compaction viscosity is different for compaction (ζ_-) and decompaction (ζ_+), then the tail is longer than the head by a factor of $\sqrt{\zeta_-/\zeta_+}$, the ratio of compaction lengths (Section 2.3). Connolly & Podladchikov (2007) took a central estimate of 30 for this factor, in which case the resulting waves have the form shown in **Figure 7**: channel-like structures with elevated porosity surrounded by a compacted sheath.

Such channel structures would focus porous flow and hence increase its speed. They would promote reactive melting and dunite formation in a cylindrical geometry. This coupling with reactive melt extraction has not been investigated.

The hypothesized asymmetry of decompaction is a yield-stress behavior. Such behavior is clearly applicable to soils and poorly consolidated sediments, where yielding depends on the effective pressure, which is proportional to the interphase pressure difference. At the high temperatures prevalent in the mantle, however, textural equilibrium is maintained on a timescale of ~30 years (Section 2). In textural equilibrium, incremental adjustments to interphase pressure differences should be symmetrical with respect to the sign of the difference. The conditions under which decompaction yielding can break textural equilibrium, and hence this symmetry, are unknown and require further research. However, processes that create sufficiently rapid variations in melt pressure could potentially nucleate viscoplastic solitary waves. This viscoplastic theory has been elaborated by Keller et al. (2013) and Yarushina & Podladchikov (2015) and is discussed further in the context of lithospheric magmatism (Section 4.3).

3.3. Climate Cycles, Sea Level, and Magmatism

The increase of Icelandic volcanism during the last deglaciation (Section 3.1.2) is consistent with the contemporaneous global trend of increased eruption rates of glaciated subaerial volcanoes (Huybers & Langmuir 2009). Glacial cycles are also cycles of SL variation, and so they may affect the submarine MOR system, which is the volumetrically dominant output of magma from

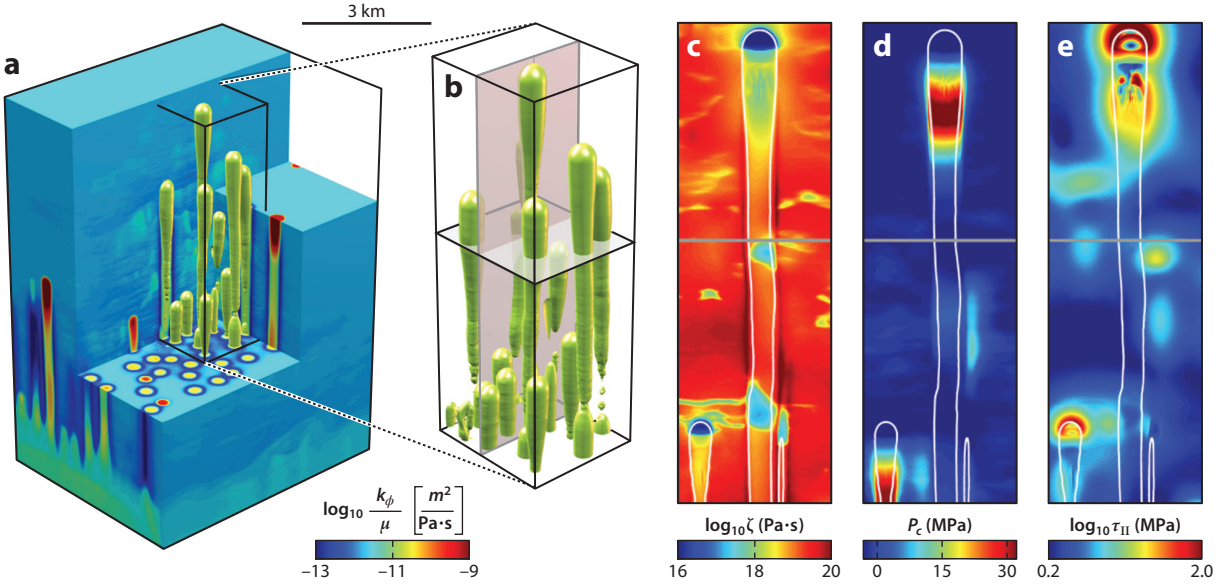

Figure 7

High-resolution 3D model of bouyancy-driven segregation with decompaction yielding presenting gravity-aligned, melt-rich channels. Results rescaled from Räss et al. (2018) to properties of partial melt in the mantle [$\phi_0 = 0.01$, $\zeta_0 = 10^{20}$ Pa s, $k_{\phi_0}/\mu_0 = 1.25 \times 10^{-14}$ m^2/(Pa s), $\delta_0 = 1.12$ km]. (*a*) Colors showing Darcy coefficient k/μ, with warm colors indicating localization in melt content and hence melt speed. (*b*) Isosurfaces of k/μ outlining channel geometry. Vertical cross sections taken along the gray plane in panel *b* show compaction viscosity, ζ, in panel *c* is weakened where compaction pressure, $P_c = (1-\phi)(P_s - P_\ell)$, in panel *d* is negative and shear stress magnitude, τ_{II}, in panel *e* is elevated. Figure adapted from Räss et al. (2018) (CC BY 4.0).

the mantle. Deglaciation increases SL, which in turn suppresses MOR magmatism. Huybers & Langmuir (2009) hypothesized that MOR magmatism is modulated by glacial cycles, and this idea was subsequently investigated by Lund & Asimow (2011), Crowley et al. (2014), and Cerpa et al. (2019a); our present discussion is based on these papers, with a particular focus on the last one. We highlight the control of the speed of melt extraction on the magmatic response to changes in SL.

The plausibility of a SL control on MOR magmatism is indicated by the following scaling argument (Lund & Asimow 2011). Background decompression melting beneath a MOR occurs at a rate proportional to $\rho_s g W_0$, whereas modulations of the melting rate are proportional to the pressure rate of SL variation $\rho_w g \Delta S/\Delta t$, where ρ_w is the density of water. A typical upwelling rate is $W_0 \sim 3$ cm/year, whereas deglaciation can cause an increase in SL of $\Delta s \sim 100$ m over $\Delta t \sim 10$ kyr. The ratio of SL perturbations to background decompression rates is thus approximately 10%, a level at which one might expect observable consequences.

To understand this system in more detail, we first consider forcing by a monochromatic, sinusoidal SL variation with period t_{SL}. It is helpful to quantify the magmatic response in terms of the amplitude ratio of ridge-axis magma supply to the SL forcing. This ratio is termed the admittance and is plotted as a function of frequency $1/t_{SL}$ in **Figure 8*a***. The melting rate is enhanced in proportion to the rate of decrease of SL, $-\dot{S}$. Therefore, if melt transport were instantaneous, there would be zero lag between this rate and the magma supply fluctuations at the ridge axis. The lag predicted on the basis of monochromatic forcing and finite melt-transport speed is plotted in **Figure 8*b*** as a function of frequency.

We now explain the behavior shown in these graphs. The SL-enhanced melting rate affects admittance via two mechanisms: (*a*) an instantaneous local change of porosity and hence melt flux

Monochromatic sinusoidal sea-level variation: a sinusoidal deviation from the mean, where ΔS is the peak-to-trough amplitude and t_{SL} is the period

Admittance: ratio of maximum amplitude of fluctuating melt flux to the mean melt flux per unit of sea-level forcing

Lag: Time between the peak rate of sea-level drop ($-\dot{S}$) and the subsequent peak in melt flux

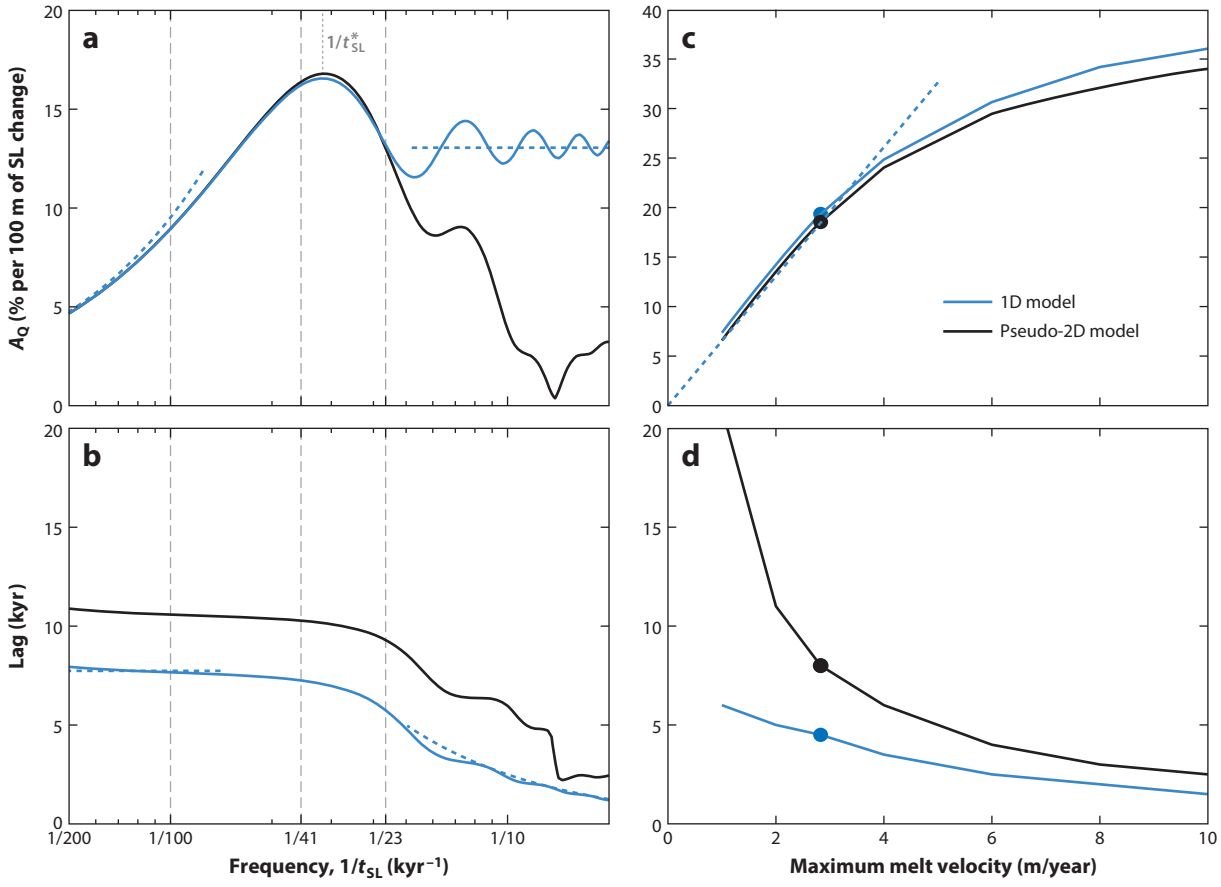

Figure 8

Magmatic response of the (dry) MOR melting region to SL variation, computed with reference parameters of Cerpa et al. (2019a), including $H = 65$ km and $W_0 = 2$ cm/year. Blue curves show results from the 1D column model; solid black curves show results from a pseudo-2D model that incorporates lateral melt focusing at a finite rate. Vertical gray dashed lines mark Milankovitch orbital frequencies. Dotted blue lines in panel *a* are the solutions at small and large frequencies (Equation 7). Panels *a* and *b* show the response spectrum to a monochromatic, sinusoidal SL forcing using a reference melt speed w_0 of 2.8 m/year. Compare to figure 2*a* of Crowley et al. (2014). Panels *c* and *d* show the average response to broadband forcing by reconstructed Pleistocene SL, as a function of w_0. Filled circles indicate the value of w_0 used to compute panels *a* and *b*. The blue dotted line in panel *c* represents the high-frequency limit in Equation 7 with $\Delta S = 125$ m. For further details, see Cerpa et al. (2019a). Abbreviations: MOR, mid-ocean ridge; SL, sea level. Figure adapted with permission from Cerpa et al. (2019a).

and (*b*) the time-dependent segregation of the additional melt generated. At low frequencies, the admittance increases in proportion to the melting-rate forcing, which scales with SL frequency. In this limit, mechanism *a* is negligible and the extra melt segregation is proportional to the forcing by mechanism *b*. Hence, the melt flux at the top of the column is in phase with $-\dot{S}$. At high frequencies, the admittance tends to a frequency-independent value. In this limit, melt segregation (mechanism *b*) over one period is negligible and the SL amplitude determines the amplitude of the porosity perturbation. The melt flux admittance is a factor n larger than that of porosity due to the permeability–porosity relationship (Section 2.1). In this limit, melt flux at the top of the column is in phase with $-S$, which peaks a quarter of a period later than its derivative, $-\dot{S}$. These physical considerations lead to the following estimates, which agree well with the numerical calculations

in **Figure 8**:

$$A_Q \approx \begin{cases} 2\pi \frac{\rho_w}{\rho_s} \frac{\Delta S}{W_0} \frac{1}{t_{SL}}, \\ n \frac{\rho_w}{\rho_s} \frac{\Delta S}{W_0} \frac{w_0}{H}, \end{cases} \quad \text{Lag} \approx \begin{cases} \frac{1}{n+1} \frac{H}{w_0}, & t_{SL} \gg t^*_{SL} \text{ (low frequency)}, \\ \frac{t_{SL}}{4}, & t_{SL} \lesssim t^*_{SL} \text{ (high frequency)}, \end{cases} \quad 7.$$

where t^*_{SL} is the critical SL forcing period that gives the maximum admittance.

The maximum admittance is attained when the contribution from the instantaneous change in porosity (mechanism *a*) is reinforced by an enhanced flux of melt segregating from below (mechanism *b*). In particular, reinforcement occurs when the period t_{SL} is a $O(1)$ multiple of the melt-travel timescale H/w_0, such that the two mechanisms constructively interfere. When $t_{SL} = t^*_{SL}$, the admittance is an $O(1)$ multiple higher than the admittance in the high-frequency limit (**Figure 8*a***). Quantitative estimates of these multiples are affected by n (Cerpa et al. 2019a).

Focusing of melts produced off axis is necessary to explain the crustal thickness and chemistry of MORs. Pseudo-2D calculations (black curves in **Figure 8**) show that lateral transport increases the predicted lag at all frequencies. The admittance at high frequency is reduced due to cancellation of perturbations of the opposite sign. However, at the lower frequencies relevant for glacial cycles, the admittance is essentially unaffected. Therefore, for monochromatic forcing, the peak admittance scales with w_0/W_0 in both 1D and pseudo-2D models.

Figure 8*c,d* show the average admittance and lag, respectively, obtained by Cerpa et al. (2019a) when forcing the model with a Pleistocene SL reconstruction. The spectrum of reconstructed SL is broad; in calculations with different values of maximum melt speed w_0, the admittance curve will align differently with this spectrum. At $w_0 \lesssim 4$ m/year, a significant part of the forcing energy is in the high-frequency regime, where $A_Q \propto w_0$ (Equation 7). In contrast, for larger w_0 (which corresponds to larger peak-response frequency $1/t^*_{SL}$), an increasing portion of the forcing energy is shifted into the low-frequency regime, where the admittance is diminished. This explains the trends in **Figure 8*c***. Faster melt-transport speed w_0 has a direct effect on the lag, reducing it as shown in **Figure 8*d***. Melt-transport speeds of ~30 m/year, as inferred in Section 3.1, should confer larger admittance but smaller lag; implications are discussed in the sidebar titled Implications of Magmatic Variation with Glacial Cycles.

4. CURRENT FRONTIERS OF RESEARCH

4.1. Subduction-Zone Magmatism

Rather less is known about the style of melt extraction in subduction zones than at MORs. Where is melt generated, and how is this process related to devolatilization of the slab? What are the pathways of melt migration? Addressing these questions will help us to understand the relative narrowness of the volcanic arc compared to the range of depths of fluid release. Seismic and especially magnetotelluric imaging have been used to infer a broad zone of partial melting and a lateral component of melt migration. A further question closely related to magmatism is, What proportion of subducted volatile elements such as carbon is transported to the deep mantle? The global carbon cycle over geological timescales crucially depends on this.

Fluid and melt migration through the mantle wedge in subduction zones is subject to the same physical processes as at MORs: buoyancy-driven porous rise, (de)compaction and attendant pressure gradients, plate-driven mantle flow, melting, and—potentially—reactive channelization, particularly that driven by volatiles. However, there are important differences relative to MORs, as discussed below. The permeability structure of the mantle crucially affects melt migration. Cagnioncle et al. (2007) showed that varying a prescribed grain size, and hence permeability, controls whether melts are dragged down with the mantle atop the slab or rise buoyantly through the mantle wedge. They speculated that melts migrate laterally along a decompaction channel at

IMPLICATIONS OF MAGMATIC VARIATION WITH GLACIAL CYCLES

Hydrothermal Venting, Crustal Thickness, and Abyssal-Hill Topography

Chemical analysis of sediment cores (Lund & Asimow 2011, Lund et al. 2016, Middleton et al. 2016, Costa et al. 2017), seismic profiling of oceanic crust (Boulahanis et al. 2020), and spectral analysis of bathymetric transects (Crowley et al. 2014, Huybers et al. 2016) provide tentative support for the hypothesis that hydrothermal venting, crustal thickness, and abyssal-hill topography, respectively, are affected by sea-level (SL)-driven variations in magma supply. Abyssal hills, however, are predominantly associated with normal faults (Goff 2015, Olive et al. 2015); the existence and nature of a relationship between normal-fault spacing and variations in magma supply at timescales of glacial cycles remain unclear (Huybers et al. 2016).

Climate Feedbacks

Glaciated volcanoes release excess CO_2 during deglaciations, which may create a positive feedback on climate warming (Huybers & Langmuir 2009). Submarine volcanoes would undergo excess degassing with some lag after glaciations [drops in SL (**Figure 8**)], which may create a negative feedback on climate cooling (Huybers & Langmuir 2009, Tolstoy 2015). This has been addressed using simplified, low-dimensional climate models (Huybers et al. 2016, Köhler & Munhoven 2020) but remains somewhat speculative. For mid-ocean ridge carbon to pace glacial cycles, its lag behind $-\dot{S}$ should be greater than about 10 ka, which is unlikely if melt transport is as rapid as expected from observational constraints (Section 3.1; **Figure 8*d***).

the base of the lithosphere, as is thought to occur at MORs. Wilson et al. (2014) included the effects of compaction on fluid flow and showed the emergence of a decompaction channel, which can lead to melt focusing toward the volcanic arc (England & Katz 2010, Ha et al. 2020). The behavior of this kind of model is sensitive to choices of material properties (Cerpa et al. 2017, 2019b). These models are poro-viscous and so do not account for the brittle processes discussed in Section 4.2.

Arguably, the most important limitations of our current understanding relate to the melting process itself, which can differ significantly from that of MORs. Melting is driven by the flux of volatiles and subducted sediments into the mantle wedge, as well as by decompression. Volatiles and sediments have a major effect on melting and rheology, and therefore it is crucial to accurately account for their migration. Instead, thermal models that account only for the flow of the mantle are widely used for subduction zones. Such models typically have a thermal structure 200–300 K cooler than that inferred from observations (Kelemen et al. 2003). Rees Jones et al. (2018) performed 2D numerical simulations with an additional prescribed melt flow, showing that melt flow alters the thermal structure of subduction zones (**Figure 9*c***), further evidence of the strongly coupled nature of subduction-zone dynamics. This study also proposed a simple model of volatile-driven melting and used it in pseudo-1D calculations, showing the evolution of melt fraction and temperature along a pathway that traverses the hot core of the mantle wedge and extends through the lithosphere to the surface. These ideas should be tested in higher-dimensional models of self-consistent, two-phase flow.

Rawson et al. (2016) hypothesized that some features of chemical variability in arc magmas are evidence of volatile-driven reactive channeling in the mantle wedge. Others have argued for diapirism as a central mechanism for melt production (e.g., Marschall & Schumacher 2012, Zhang et al. 2020). However, at this stage there are no published 2D models that account for the coupling between volatile-driven melting, melt segregation and compaction, and two-phase thermal

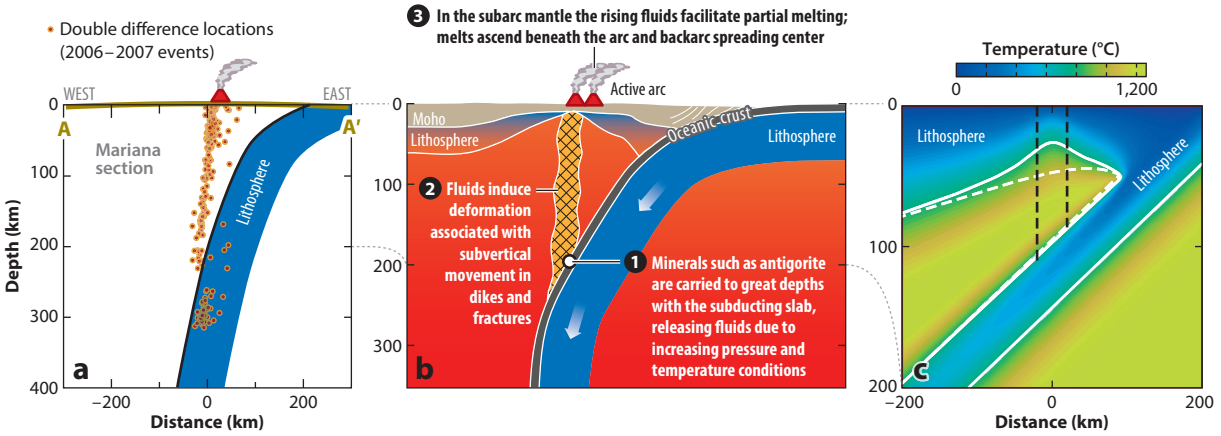

Figure 9

Fluid and thermal transport in subduction zones. (*a*) Earthquake swarm located within the subduction-zone mantle wedge of the Mariana Arc, projected from ±20 km perpendicular to the section. Panel *a* adapted from White et al. (2019) (CC BY 4.0). (*b*) Schematic diagram explaining the fluid-driven-fracture hypothesis. Panel *b* adapted from White et al. (2019) (CC BY 4.0). (*c*) Subduction-zone thermal structure as modified by fluid transport of heat. White contours are 800°C isotherms, with fluid transport (*solid lines*) and without (*dashed lines*). The imposed Darcian fluid flow is vertical, between the black dashed lines. It has a Gaussian horizontal profile centered at $x = 0$ and a half-width of 10 km. The maximum vertical Darcy flux is $\phi w_0 = 3$ m/kyr. Panel *c* adapted with permission from Rees Jones et al. (2018).

and chemical transport throughout the mantle wedge. This is a key challenge for future modeling and a place where realistic thermochemistry should be coupled with the dynamics of melt migration.

4.2. Ascent Through Brittle Fracture

Is fluid-driven fracture a viable and relevant mechanism for melt transport through the asthenosphere? This was considered plausible but unlikely in the review by Kelemen et al. (1997). The challenge remains in understanding the conditions under which asthenospheric dikes could occur and whether those conditions prevail anywhere. The key criterion is a liquid pressure that exceeds the minimum compressive stress by the cohesive strength of the rock. To achieve a large and localized liquid overpressure, the timescale of the process creating the overpressure must be short relative to the Maxwell time, which is of order 10 years in the hot asthenosphere.

Earthquake swarms located within the mantle wedge beneath volcanic arcs provide new evidence that fluid-driven fracture of the asthenosphere is possible (White et al. 2019). **Figure 9*a*** shows carefully relocated hypocenters from a swarm in the Mariana Arc, projected onto the diagram from within ±20 km to the transect. The events form an array connecting the slab to the surface. In this case, no evidence of volcanic activity is found at the surface above the array. In contrast, for a different swarm at the Izu-Bonin Arc, the array terminates beneath an active volcano. Centroid moment tensor solutions, computed for the Mariana case only, show double-couple contributions between 10% and 50%. In most cases, the other contribution is from a vertical dipole moment, indicating a net downward acceleration of mass at the source. White et al. (2019) attributed these swarms to high-pressure migration by fluid-driven fracture (**Figure 9*b***). They applied a sequence analysis to argue for a melt-transport speed of order 1 km/h, which is similar to volcanic ascent rates but much faster than indicated by U-series disequilibria or models of channelized flow.

Maxwell time: the timescale τ over which a viscoelastic medium relaxes elastic stress by irreversible, viscous flow; $\tau = \eta/E$, where η is the dynamic viscosity and E is the elastic modulus

If these interpretations are correct, questions are raised about the relative importance of this mode of transport, the details of the mechanics in situ, and the extent to which these mechanics apply in other settings. Sudden fluid release from the cold, brittle slab may create a local overpressure at the base of the wedge and initiate a fracture sequence (Davies 1999). But many questions remain unanswered. Does this process depend on the cool wedge temperatures above the slab and on the low viscosity and low density of the slab-derived liquid? How do the temperature and composition of fluids evolve as they traverse the wedge within fractures? These observations also raise questions with broader relevance. For example, can silicate melts formed during decompression of fertile, volatile-rich mantle heterogeneities induce fracture? And most importantly, does the absence of recorded seismic swarms in the asthenosphere beneath MORs and hotspot volcanoes imply an absence of fluid-driven fracture there? These questions should motivate further investigation of asthenospheric sources of seismic energy, as well as mechanical models incorporating elasticity and fluid-driven brittle failure (e.g., Keller et al. 2013; see below).

4.3. Melt at the Lithosphere–Asthenosphere Boundary and in the Lithosphere

Melt ascent does not (always) terminate at the LAB, the thermal boundary where the conduction-dominated, near-surface geotherm steepens with depth into the convection-dominated mantle adiabat (see Rychert et al. 2020). Initially, mantle melt ascending to the LAB will freeze where the temperature decreases below the liquidus of the melt. Crystallization releases latent heat and adds fertile minerals (e.g., pyroxene) into previously cool and refractory mantle lithosphere. This could drive the crystallization front to migrate upward, moving the LAB with it. If melt supply from the asthenosphere is localized, then this upward migration may establish an undulating permeability boundary (Katz 2008). A decompaction channel beneath this boundary could enhance focusing toward its high points (see also Section 4.1). Magnetotelluric resistivity imaging has recently produced evidence of possible LAB thermal erosion by melt infiltration near the Mid-Atlantic Ridge (Wang et al. 2020) and beneath an intraplate volcanic field in Northeast China (Li et al. 2021).

At high points of the LAB, melts may accumulate to fractions greater than 10%, well above that of the mantle source region (<1%). They may also differentiate to compositions richer in silica, volatiles, and incompatible elements (Macpherson et al. 2006, Collier & Kelemen 2010, Jackson et al. 2018). This process had been inferred from geological evidence and described as melting, assimilation, storage, and homogenization (Hildreth & Moorbath 1988) or as a deep crustal hot zone (Annen et al. 2006), although these have focused on the lower crust, not the mantle lithosphere. Toward a more quantitative description, Keller & Suckale (2019) derived a mixture-theory framework to model the transition from low-ϕ porous flow to high-ϕ mushy and suspension flows. The broad interpretation of these magmatic systems is that over time, vertically extensive mush columns develop from which melt-rich magma is extracted to feed volcanic activity (Bachmann & Huber 2019), while the residual crystal-rich mush solidifies into a plutonic rock complex (Cashman et al. 2017). Questions remain, however: What are the origin, spatial extent, and distribution of melt-accumulating undulations of the LAB? Does melt reach crustal levels by steady migration of the crystallization front or by punctuated, fluid-driven fracture from near the LAB?

Answering the latter question requires an understanding of melt interaction with the rheological transition from ductile to elastic–brittle deformation across the lithosphere. The Maxwell time (Section 4.2) increases along the ascent path into cooler rock, which is favorable for fracture. However, melt accumulation at the LAB locally weakens the rock matrix and decreases the Maxwell time, and hence stress may be relaxed before it builds to the point of fracture. Havlin et al. (2013), addressing this problem directly, used a model of dike propagation from the LAB

to argue that melt drains into dikes before it accumulates to the point of solid disaggregation or stress relaxation. Other work has been less focused on specific details of the LAB. Keller et al. (2013) and Yarushina et al. (2015, 2020) extended the poro-viscous theory of McKenzie (1984) with a viscoelastic–plastic matrix rheology. Where the cohesive–frictional yield criterion dips to less than 10 MPa under decompaction, the models produce a decompaction weakening effect (Connolly & Podladchikov 2007) with an additional dependence on shear stress (Yarushina et al. 2020). At intermediate shear stress, stress-aligned melt-rich bands can emerge, while at higher shear stress, dike-like localization features become possible (Keller et al. 2013). Further work is needed to understand and validate this rheological formulation in the context of two-phase flow through the lithosphere.

4.4. Coupling Petrological Thermodynamics

Chemical thermodynamics is central to the physics of magmatism but has generally been investigated in isolation from the mechanics. The preceding discussion of the relationship between mantle heterogeneity, volatile elements, thermal diffusion, and channelized flow indicates that thermochemistry and mechanics may be tightly coupled. Investigating this coupling with parameterized thermochemistry (e.g., **Figure 5**) risks missing important interactions between flow, chemical transport, and reactions. Transport properties (viscosities, permeability) depend on phase compositions in important and unexplored ways. Moreover, a wealth of existing observations of melts and solid residues could be used to test models that make quantitative petrological predictions.

Incorporating fully detailed mantle thermochemistry is difficult, however. It calls for tracking at least 10 chemical components in approximately 5 distinct mineral phases, plus the liquid phase. Determining the equilibrium state requires a free-energy minimization within a large parameter space. The natural system may depart from equilibrium, motivating an additional kinetic theory. Both equilibrium and disequilibrium calculations require empirical thermodynamic data over a vast space of composition, temperature, and pressure. Despite large and growing thermodynamic databases, significant regions of the space remain poorly constrained.

The equilibrium approach has generally involved coupling an existing thermochemical solver for Gibbs-free-energy minimization with a formulation of multiphase fluid mechanics. As examples, Tirone & Sessing (2017) used AlphaMELTS and Oliveira et al. (2020) used Perple_X (see those papers for references to the thermodynamic models). This approach comes with significant computational costs that may be partially mitigated by dynamic optimizations. Other work has focused on development of a theoretical framework for disequilibrium phase change (Šrámek et al. 2007, Rudge et al. 2011), based on irreversible thermodynamics. This has been adapted and used in parameterized thermochemical models (e.g., Keller & Katz 2016, Keller et al. 2017). However, the disequilibrium approach requires calculation of the equilibrium state; with the full set of mantle components, this carries the same costs as for equilibrium thermochemistry. The ENKI project (**http://enki-portal.org**) aims to provide a platform for rigorous thermochemistry that is computationally efficient, open source, and flexible in the choice of thermochemical components. It has been used to model the opx–olivine peritectic and incorporated into a model of magmatic segregation that predicts the formation of channels and dunite bodies (Tweed 2021).

Inclusion of full mantle thermochemistry into models of magma segregation promises to expose natural feedbacks on the fluid mechanics and to make predictions that are testable against petrological observations. In practice, however, this is far from straightforward: Inaccuracies in thermodynamic calculations can lead to physical artefacts, computational costs may require problematic sacrifices elsewhere (e.g., grid resolution, parameter space), initial and boundary conditions become more complex, and model outputs may be difficult to understand in simple terms

(and hence validate). Therefore, while detailed thermochemistry is a frontier of research in the physics of melt extraction, it will not supplant simpler, reduced models anytime soon.

SUMMARY POINTS

1. Observational constraints on the speed of buoyancy-driven melt extraction from upwelling asthenosphere indicate that it is ~30 m/year, faster than can be explained by diffuse porous flow.
2. These observations are consistent with a style of flow in which melt flux is concentrated into high-permeability channels. The channels arise by a reactive flow instability. Mantle heterogeneity, thermal diffusion, and decompaction weakening may reinforce this instability.
3. Quantitative details of the reactive instability depend on material properties, the most important of which are permeability, compaction viscosity, and the chemical thermodynamics of melting and reaction.
4. Pressure variations associated with sea level may drive a variation of greater than ~10% in submarine melt extraction, with a lag of ~1 ka between forcing and response. If so, this has potentially observable implications.
5. Melt formation, reactive flow, and extraction at subduction zones are challenging problems due to the petrological and dynamic complexity. Observations of seismic swarms traversing the mantle wedge are evidence for fluid-driven fracture as a mode of transport. This mode is likely an exception, rather than the norm.
6. Coupling melt transport to realistic petrological thermodynamics will improve our understanding of reactive melting and melt extraction. Coupling melt transport to low-temperature rheological models will improve our understanding of melt extraction through the lithosphere and the mechanical role of magma at plate boundaries.

FUTURE ISSUES

1. How are melt geometry, grain-size evolution, and rheological properties affected by deviatoric stress and polymineralogy of mantle rocks?
2. What is the relationship between magmatic segregation and reactive channelization in the context of the fully detailed chemical thermodynamics of the asthenosphere, including volatiles?
3. What is the relationship between mantle heterogeneity, melt production, and melt segregation, and what are the observable consequences of this?
4. What is the role, if any, of fluid-driven fracture, decompaction weakening, or yielding in asthenospheric melt transport?
5. What is the distribution of melting and melt transport in subduction zones, and how does this distribution feed back on thermal structure, arc position, volatile recycling, and the chemistry of arc magmatism?
6. How does magma interact with the lithosphere–asthenosphere boundary, and how does it traverse the lithosphere?

DISCLOSURE STATEMENT

The authors are not aware of any affiliations, memberships, funding, or financial holdings that might be perceived as affecting the objectivity of this review.

ACKNOWLEDGMENTS

The authors acknowledge helpful discussions with O. Shorttle, M. Spiegelman, A. Stracke, and L. Tweed. Comments by G. Hirth and P. Kelemen and an editorial review by R. Rudnick helped to refine the manuscript. This research received funding from the European Research Council under Horizon 2020 research and innovation program grant agreement 772255. The authors thank the Isaac Newton Institute for Mathematical Sciences for its hospitality during the program Melt in the Mantle, which was supported by EPSRC grant EP/K032208/1. D.W.R.J. acknowledges research funding through the NERC (Natural Environment Research Council) Consortium grant NE/M000427/1 and through the Leverhulme Trust.

LITERATURE CITED

Aharonov E, Whitehead JA, Kelemen PB, Spiegelman M. 1995. Channeling instability of upwelling melt in the mantle. *J. Geophys. Res.* 100(B10):20433–50

Annen C, Blundy J, Sparks R. 2006. The genesis of intermediate and silicic magmas in deep crustal hot zones. *J. Petrol.* 47:505–39

Austin NJ, Evans B. 2007. Paleowattmeters: a scaling relation for dynamically recrystallized grain size. *Geology* 35:343–46

Bachmann O, Huber C. 2019. The inner workings of crustal distillation columns; the physical mechanisms and rates controlling phase separation in silicic magma reservoirs. *J. Petrol.* 60:3–18

Baltzell C, Parmentier EM, Liang Y, Tirupathi S. 2015. A high-order numerical study of reactive dissolution in an upwelling heterogeneous mantle: 2. Effect of shear deformation. *Geochem. Geophys. Geosyst.* 16:3855–69

Bercovici D, Ricard Y. 2012. Mechanisms for the generation of plate tectonics by two-phase grain-damage and pinning. *Phys. Earth Planet. Inter.* 202–203:27–55

Bercovici D, Ricard Y, Schubert G. 2001. A two-phase model for compaction and damage: 1. General theory. *J. Geophys. Res.* 106(B5):8887–906

Bo T, Katz RF, Shorttle O, Rudge JF. 2018. The melting column as a filter of mantle trace-element heterogeneity. *Geochem. Geophys. Geosyst.* 19:4694–721

Boulahanis B, Carbotte SM, Huybers PJ, Nedimović MR, Aghaei O, et al. 2020. Do sea level variations influence mid-ocean ridge magma supply? A test using crustal thickness and bathymetry data from the East Pacific Rise. *Earth Planet. Sci. Lett.* 535:116121

Braun MG, Kelemen PB. 2002. Dunite distribution in the Oman ophiolite: implications for melt flux through porous dunite conduits. *Geochem. Geophys. Geosyst.* 3:8603

Breithaupt T, Hansen LN, Toppaladoddi S, Katz RF. 2021. The role of grain-environment heterogeneity in normal grain growth: a stochastic approach. *Acta Mater.* 209:116699

Butler SL. 2009. The effects of buoyancy on shear-induced melt bands in a compacting porous medium. *Phys. Earth Planet. Inter.* 173:51–59

Butler SL. 2012. Numerical models of shear-induced melt band formation with anisotropic matrix viscosity. *Phys. Earth Planet. Inter.* 200:28–36

Butler SL. 2017. Shear-induced porosity bands in a compacting porous medium with damage rheology. *Phys. Earth Planet. Inter.* 264:7–17

Cagnioncle AM, Parmentier E, Elkins-Tanton L. 2007. Effect of solid flow above a subducting slab on water distribution and melting at convergent plate boundaries. *J. Geophys. Res.* 112(B9):B09402

Cashman KV, Sparks RSJ, Blundy JD. 2017. Vertically extensive and unstable magmatic systems: a unified view of igneous processes. *Science* 355(6331):eaag3055

Cerpa NG, Rees Jones DW, Katz RF. 2019a. Consequences of glacial cycles for magmatism and carbon transport at mid-ocean ridges. *Earth Planet. Sci. Lett.* 528:115845

Cerpa NG, Wada I, Wilson CR. 2017. Fluid migration in the mantle wedge: influence of mineral grain size and mantle compaction. *J. Geophys. Res. Solid Earth* 122:6247–68

Cerpa NG, Wada I, Wilson CR. 2019b. Effects of fluid influx, fluid viscosity, and fluid density on fluid migration in the mantle wedge and their implications for hydrous melting. *Geosphere* 15:1–23

Collier ML, Kelemen PB. 2010. The case for reactive crystallization at mid-ocean ridges. *J. Petrol.* 51:1913–40

Connolly JAD, Podladchikov YY. 1998. Compaction-driven fluid flow in viscoelastic rock. *Geodin. Acta* 11:55–84

Connolly JAD, Podladchikov YY. 2007. Decompaction weakening and channeling instability in ductile porous media: implications for asthenospheric melt segregation. *J. Geophys. Res.* 112(B10):B10205

Connolly JAD, Schmidt MW, Solferino G, Bagdassarov N. 2009. Permeability of asthenospheric mantle and melt extraction rates at mid-ocean ridges. *Nature* 462:209–12

Cooper RF. 1990. Differential stress-induced melt migration: an experimental approach. *J. Geophys. Res.* 95(B5):6979–92

Cooper RF, Kohlstedt DL. 1984. Solution-precipitation enhanced diffusional creep of partially molten olivine-basalt aggregates during hot-pressing. *Tectonophysics* 107:207–33

Cooper RF, Kohlstedt DL. 1986. Rheology and structure of olivine-basalt partial melts. *J. Geophys. Res.* 91(B9):9315–23

Costa KM, McManus JF, Middleton JL, Langmuir CH, Huybers P, et al. 2017. Hydrothermal deposition on the Juan de Fuca Ridge over multiple glacial-interglacial cycles. *Earth Planet. Sci. Lett.* 479:120–32

Crowley JW, Katz RF, Huybers P, Langmuir CH, Park SH. 2014. Glacial cycles drive variations in the production of oceanic crust. *Science* 347:1237–40

Davies JH. 1999. The role of hydraulic fractures and intermediate-depth earthquakes in generating subduction-zone magmatism. *Nature* 398:142–45

Eason DE, Sinton JM, Grönvold K, Kurz MD. 2015. Effects of deglaciation on the petrology and eruptive history of the Western Volcanic Zone, Iceland. *Bull. Volcanol.* 77:47

Eksinchol I, Rudge JF, Maclennan J. 2019. Rate of melt ascent beneath Iceland from the magmatic response to deglaciation. *Geochem. Geophys. Geosyst.* 20:2585–605

Elkins LJ, Bourdon B, Lambart S. 2019. Testing pyroxenite versus peridotite sources for marine basalts using U-series isotopes. *Lithos* 332:226–44

Elliott T, Spiegelman MW. 2003. Melt migration in oceanic crustal production: a U-series perspective. In *Treatise on Geochemistry*, ed. KK Turekian, HD Holland, pp. 465–510. Amsterdam: Elsevier

England PC, Katz RF. 2010. Melting above the anhydrous solidus controls the location of volcanic arcs. *Nature* 467:700–3

Faul UH, Jackson I. 2007. Diffusion creep of dry, melt-free olivine. *J. Geophys. Res.* 112(B4):B04204

Fowler AC. 1984. On the transport of moisture in polythermal glaciers. *Geophys. Astrophys. Fluid Dyn.* 28:99–140

Gebhardt D, Butler S. 2016. Linear analysis of melt band formation in a mid-ocean ridge corner flow. *Geophys. Res. Lett.* 43:3700–7

Ghods A, Arkani-Hamed J. 2000. Melt migration beneath mid-ocean ridges. *Geophys. J. Int.* 140:687–97

Goff JA. 2015. Comment on "Glacial cycles drive variations in the production of oceanic crust." *Science* 349:1065

Ha G, Montési LG, Zhu W. 2020. Melt focusing along permeability barriers at subduction zones and the location of volcanic arcs. *Geochem. Geophys. Geosyst.* 21:e2020GC009253

Hansen LN, Warren JM. 2015. Quantifying the effect of pyroxene on deformation of peridotite in a natural shear zone. *J. Geophys. Res. Solid Earth* 120:2717–38

Havlin C, Parmentier E, Hirth G. 2013. Dike propagation driven by melt accumulation at the lithosphere–asthenosphere boundary. *Earth Planet. Sci. Lett.* 376:20–28

Hesse MA, Schiemenz AR, Liang Y, Parmentier EM. 2011. Compaction-dissolution waves in an upwelling mantle column. *Geophys. J. Int.* 187:1057–75

Hewitt IJ. 2010. Modelling melting rates in upwelling mantle. *Earth Planet. Sci. Lett.* 300:264–74

Hewitt IJ, Fowler AC. 2008. Partial melting in an upwelling mantle column. *Proc. R. Soc. A* 464:2467–91

Hildreth W, Moorbath S. 1988. Crustal contributions to arc magmatism in the Andes of central Chile. *Contrib. Mineral. Petrol.* 98:455–89

Hirschmann MM, Stolper EM. 1996. A possible role for garnet pyroxenite in the origin of the "garnet signature" in MORB. *Contrib. Mineral. Petrol.* 124:185–208

Holness M, Siklos S. 2000. The rates and extent of textural equilibration in high-temperature fluid-bearing systems. *Chem. Geol.* 162:137–53

Holtzman B, Groebner N, Zimmerman M, Ginsberg S, Kohlstedt D. 2003. Stress-driven melt segregation in partially molten rocks. *Geochem. Geophys. Geosyst.* 4:8607

Huybers P, Langmuir C. 2009. Feedback between deglaciation, volcanism, and atmospheric CO_2. *Earth Planet. Sci. Lett.* 286(3–4):479–91

Huybers P, Langmuir C, Katz RF, Ferguson D, Proistosescu C, Carbotte S. 2016. Comment on "Sensitivity of seafloor bathymetry to climate-driven fluctuations in mid-ocean ridge magma supply." *Science* 352:1405

Ito G, Mahoney J. 2005. Flow and melting of a heterogeneous mantle: 1. Method and importance to the geochemistry of ocean island and mid-ocean ridge basalts. *Earth Planet. Sci. Lett.* 230:29–46

Jackson M, Blundy J, Sparks R. 2018. Chemical differentiation, cold storage and remobilization of magma in the Earth's crust. *Nature* 564:405–9

Jordan JS, Hesse MA. 2015. Reactive transport in a partially molten system with binary solid solution. *Geochem. Geophys. Geosyst.* 16:4153–77

Jull M, Kelemen P, Sims K. 2002. Consequences of diffuse and channelled porous melt migration on uranium series disequilibria. *Geochim. Cosmochim. Acta* 66(23):4133–48

Jull M, McKenzie D. 1996. The effect of deglaciation on mantle melting beneath Iceland. *J. Geophys. Res.* 101(B10):21815–28

Katz RF. 2008. Magma dynamics with the enthalpy method: benchmark solutions and magmatic focusing at mid-ocean ridges. *J. Petrol.* 49(12):2099–121

Katz RF. 2022. *The Dynamics of Partially Molten Rock*. Princeton, NJ: Princeton Univ. Press.

Katz RF, Rudge JF. 2011. The energetics of melting fertile heterogeneities within the depleted mantle. *Geochem. Geophys. Geosyst.* 12:Q0AC16

Katz RF, Spiegelman M, Holtzman B. 2006. The dynamics of melt and shear localization in partially molten aggregates. *Nature* 442:676–79

Katz RF, Weatherley S. 2012. Consequences of mantle heterogeneity for melt extraction at mid-ocean ridges. *Earth Planet. Sci. Lett.* 335–336:226–37

Kelemen PB. 1990. Reaction between ultramafic rock and fractionating basaltic magma I. Phase relations, the origin of calc-alkaline magma series, and the formation of discordant dunite. *J. Petrol.* 31:51–98

Kelemen PB, Braun M, Hirth G. 2000. Spatial distribution of melt conduits in the mantle beneath oceanic spreading ridges: observations from the Ingalls and Oman ophiolites. *Geochem. Geophys. Geosyst.* 1:1005

Kelemen PB, Dick HJB, Quick JE. 1992. Formation of hartzburgite by pervasive melt rock reaction in the upper mantle. *Nature* 358:635–41

Kelemen PB, Hirth G, Shimizu N, Spiegelman M, Dick H. 1997. A review of melt migration processes in the adiabatically upwelling mantle beneath oceanic spreading ridges. *Philos. Trans. R. Soc. A* 355:283–318

Kelemen PB, Rilling JL, Parmentier EM, Mehl L, Hacker BR. 2003. Thermal structure due to solid-state flow in the mantle wedge beneath arcs. *Geophys. Monogr. Ser.* 138:293–311

Kelemen PB, Whitehead JA, Aharonov E, Jordahl KA. 1995. Experiments on flow focusing in soluble porous media, with applications to melt extraction from the mantle. *J. Geophys. Res.* 100(B1):475–96

Keller T, Katz RF. 2016. The role of volatiles in reactive melt transport in the asthenosphere. *J. Petrol.* 57:1073–108

Keller T, Katz RF, Hirschmann MM. 2017. Volatiles beneath mid-ocean ridges: deep melting, channelised transport, focusing, and metasomatism. *Earth Planet. Sci. Lett.* 464:55–68

Keller T, May DA, Kaus BJP. 2013. Numerical modelling of magma dynamics coupled to tectonic deformation of lithosphere and crust. *Geophys. J. Int.* 195:1406–42

Keller T, Suckale J. 2019. A continuum model of multi-phase reactive transport in igneous systems. *Geophys. J. Int.* 219:185–222

Kogiso T, Hirschmann MM. 2006. Partial melting experiments of bimineralic eclogite and the role of recycled mafic oceanic crust in the genesis of ocean island basalts. *Earth Planet. Sci. Lett.* 249:188–99

Kogiso T, Hirschmann MM, Pertermann M. 2004a. High-pressure partial melting of mafic lithologies in the mantle. *J. Petrol.* 45:2407–22

Kogiso T, Hirschmann MM, Reiners P. 2004b. Length scales of mantle heterogeneities and their relationship to ocean island basalt geochemistry. *Geochim. Cosmochim. Acta* 68:345–60
Köhler P, Munhoven G. 2020. Late Pleistocene carbon cycle revisited by considering solid Earth processes. *Paleoceanogr. Paleoclimatol.* 35(12):e2020PA004020
Kohlstedt DL, Hansen LN. 2015. Constitutive equations, rheological behavior, and viscosity of rocks. In *Treatise on Geophysics*, ed. G Schubert, pp. 441–72. Oxford, UK: Elsevier. 2nd ed.
Kohlstedt DL, Holtzman BK. 2009. Shearing melt out of the Earth: an experimentalist's perspective on the influence of deformation on melt extraction. *Annu. Rev. Earth Planet. Sci.* 37:561–93
Kohlstedt DL, Zimmerman ME. 1996. Rheology of partially molten mantle rocks. *Annu. Rev. Earth Planet. Sci.* 24:41–62
Li Y, Weng A, Xu W, Zou Z, Tang Y, et al. 2021. Translithospheric magma plumbing system of intraplate volcanoes as revealed by electrical resistivity imaging. *Geology* 49(11):1337–42
Liang Y, Schiemenz A, Hesse M, Parmentier E, Hesthaven J. 2010. High-porosity channels for melt migration in the mantle: Top is the dunite and bottom is the harzburgite and lherzolite. *Geophys. Res. Lett.* 37:L15306
Liu B, Liang Y. 2019. Importance of permeability and deep channel network on the distribution of melt, fractionation of REE in abyssal peridotites, and U-series disequilibria in basalts beneath mid-ocean ridges: a numerical study using a 2D double-porosity model. *Earth Planet. Sci. Lett.* 528:115788
Longhi J. 2002. Some phase equilibrium systematics of lherzolite melting: I. *Geochem. Geophys. Geosyst.* 3:1–33
Lund DC, Asimow PD. 2011. Does sea level influence mid-ocean ridge magmatism on Milankovitch timescales? *Geochem. Geophys. Geosyst.* 12:Q12009
Lund DC, Asimow PD, Farley KA, Rooney TO, Seeley E, et al. 2016. Enhanced East Pacific Rise hydrothermal activity during the last two glacial terminations. *Science* 351:478–82
Lundstrom C, Gill J, Williams Q. 2000. A geochemically consistent hypothesis for MORB generation. *Chem. Geol.* 162:105–26
Maclennan J, Jull M, McKenzie D, Slater L, Grönvold K. 2002. The link between volcanism and deglaciation in Iceland. *Geochem. Geophys. Geosyst.* 3(11):1–25
Macpherson CG, Dreher ST, Thirlwall MF. 2006. Adakites without slab melting: high pressure differentiation of island arc magma, Mindanao, the Philippines. *Earth Planet. Sci. Lett.* 243:581–93
Marschall HR, Schumacher JC. 2012. Arc magmas sourced from mélange diapirs in subduction zones. *Nat. Geosci.* 5:862–67
McCarthy C, Takei Y. 2011. Anelasticity and viscosity of partially molten rock analogue: toward seismic detection of small quantities of melt. *Geophys. Res. Lett.* 38:L18306
McKenzie D. 1984. The generation and compaction of partially molten rock. *J. Petrol.* 25:713–65
McKenzie D. 2000. Constraints on melt generation and transport from U-series activity ratios. *Chem. Geol.* 162:81–94
Mei S, Bai W, Hiraga T, Kohlstedt D. 2002. Influence of melt on the creep behavior of olivine-basalt aggregates under hydrous conditions. *Earth Planet. Sci. Lett.* 201:491–507
Middleton JL, Langmuir CH, Mukhopadhyay S, McManus JF, Mitrovica JX. 2016. Hydrothermal iron flux variability following rapid sea level changes. *Geophys. Res. Lett.* 43:3848–56
Miller KJ, Montési LGJ, Zhu W. 2015. Estimates of olivine–basaltic melt electrical conductivity using a digital rock physics approach. *Earth Planet. Sci. Lett.* 432:332–41
Miller KJ, Zhu W, Montési LGJ, Gaetani GA. 2014. Experimental quantification of permeability of partially molten mantle rock. *Earth Planet. Sci. Lett.* 388:273–82
Miller KJ, Zhu W, Montési LGJ, Gaetani GA, Le Roux V, Xiao X. 2016. Experimental evidence for melt partitioning between olivine and orthopyroxene in partially molten harzburgite. *J. Geophys. Res. Solid Earth* 121:5776–93
Morgan Z, Liang Y. 2003. An experimental and numerical study of the kinetics of harzburgite reactive dissolution with applications to dunite dike formation. *Earth Planet. Sci. Lett.* 214:59–74
Morgan Z, Liang Y. 2005. An experimental study of the kinetics of lherzolite reactive dissolution with applications to melt channel formation. *Contrib. Mineral. Petrol.* 150:369–85
Olive JA, Behn M, Ito G, Buck W, Escartín J, Howell S. 2015. Sensitivity of seafloor bathymetry to climate-driven fluctuations in mid-ocean ridge magma supply. *Science* 350:310–13

Oliveira B, Afonso JC, Tilhac R. 2020. A disequilibrium reactive transport model for mantle magmatism. *J. Petrol.* 61(9):egaa067
Pec M, Holtzman BK, Zimmerman M, Kohlstedt DL. 2015. Reaction infiltration instabilities in experiments on partially molten mantle rocks. *Geology* 43:575–78
Pec M, Holtzman BK, Zimmerman ME, Kohlstedt DL. 2017. Reaction infiltration instabilities in mantle rocks: an experimental investigation. *J. Petrol.* 58:979–1003
Pec M, Holtzman BK, Zimmerman ME, Kohlstedt DL. 2020. Influence of lithology on reactive melt flow channelization. *Geochem. Geophys. Geosyst.* 21:e2020GC008937
Pertermann M, Hirschmann M. 2003a. Anhydrous partial melting experiments on MORB-like eclogite: phase relations, phase compositions and mineral-melt partitioning of major elements at 2–3 GPa. *J. Petrol.* 44:2173–201
Pertermann M, Hirschmann M. 2003b. Partial melting experiments on a MORB-like pyroxenite between 2 and 3 GPa: constraints on the presence of pyroxenite in basalt source regions from solidus location and melting rate. *J. Geophys. Res.* 108(B2):2125
Pilet S, Baker MB, Stolper EM. 2008. Metasomatized lithosphere and the origin of alkaline lavas. *Science* 320:916–19
Python M, Ceuleneer G. 2003. Nature and distribution of dykes and related melt migration structures in the mantle section of the Oman ophiolite. *Geochem. Geophys. Geosyst.* 4:8612
Qi C, Kohlstedt D, Katz R, Takei Y. 2015. An experimental test of the viscous anisotropy hypothesis for partially molten rocks. *PNAS* 112(41):12616–20
Räss L, Simon NS, Podladchikov YY. 2018. Spontaneous formation of fluid escape pipes from subsurface reservoirs. *Sci. Rep.* 8:11116
Rawson H, Keller T, Fontijn K, Pyle DM, Mather TA, et al. 2016. Compositional variability in mafic arc magmas over short spatial and temporal scales: evidence for the signature of mantle reactive melt channels. *Earth Planet. Sci. Lett.* 456:66–77
Rees Jones DW, Katz RF. 2018. Reaction-infiltration instability in a compacting porous medium. *J. Fluid Mech.* 852:5–36
Rees Jones DW, Katz RF, Tian M, Rudge JF. 2018. Thermal impact of magmatism in subduction zones. *Earth Planet. Sci. Lett.* 481:73–79
Rees Jones DW, Rudge JF. 2020. Fast magma ascent, revised estimates from the deglaciation of Iceland. *Earth Planet. Sci. Lett.* 542:116324
Rees Jones DW, Zhang H, Katz RF. 2021. Magmatic channelization by reactive and shear-driven instabilities at mid-ocean ridges: a combined analysis. *Geophys. J. Int.* 226:582–609
Renner J, Viskupic K, Hirth G, Evans B. 2003. Melt extraction from partially molten peridotites. *Geochem. Geophys. Geosyst.* 4:8606
Rivalta E, Taisne B, Bunger A, Katz R. 2015. A review of mechanical models of dike propagation: schools of thought, results and future directions. *Tectonophysics* 638:1–42
Rochat L, Pilet S, Müntener O, Duretz T, Baumgartner L, et al. 2017. Garnet xenocryst from petit-spot lavas as an indicator for off-axis mantle refertilization at intermediate spreading ridges. *Geology* 45:1091–94
Rubin KH, van der Zander I, Smith MC, Bergmanis EC. 2005. Minimum speed limit for ocean ridge magmatism from ^{210}Pb–^{226}Ra–^{230}Th disequilibria. *Nature* 437:534–38
Rudge JF. 2018a. Textural equilibrium melt geometries around tetrakaidecahedral grains. *Proc. R. Soc. A* 474:20170639
Rudge JF. 2018b. The viscosities of partially molten materials undergoing diffusion creep. *J. Geophys. Res. Solid Earth* 123:10534–62
Rudge JF, Bercovici D. 2015. Melt-band instabilities with two-phase damage. *Geophys. J. Int.* 201:640–51
Rudge JF, Bercovici D, Spiegelman M. 2011. Disequilibrium melting of a two phase multicomponent mantle. *Geophys. J. Int.* 184:699–718
Rychert CA, Harmon N, Constable S, Wang S. 2020. The nature of the lithosphere-asthenosphere boundary. *J. Geophys. Res. Solid Earth* 125:e2018JB016463
Schiemenz A, Liang Y, Parmentier EM. 2011. A high-order numerical study of reactive dissolution in an upwelling heterogeneous mantle—I. Channelization, channel lithology and channel geometry. *Geophys. J. Int.* 186:641–64

Schmeling H, Kruse JP, Richard G. 2012. Effective shear and bulk viscosity of partially molten rock based on elastic moduli theory of a fluid filled poroelastic medium. *Geophys. J. Int.* 190:1571–78

Scott DR, Stevenson DJ. 1986. Magma ascent by porous flow. *J. Geophys. Res.* 91(B9):9283–96

Scott T, Kohlstedt D. 2006. The effect of large melt fraction on the deformation behavior of peridotite. *Earth Planet. Sci. Lett.* 246:177–87

Shorttle O, Maclennan J, Lambart S. 2014. Quantifying lithological variability in the mantle. *Earth Planet. Sci. Lett.* 395:24–40

Sim SJ, Spiegelman M, Stegman DR, Wilson C. 2020. The influence of spreading rate and permeability on melt focusing beneath mid-ocean ridges. *Phys. Earth Planet. Inter.* 304:106486

Simpson G, Spiegelman M, Weinstein M. 2010a. A multiscale model of partial melts: 1. Effective equations. *J. Geophys. Res.* 115(B4):B04410

Simpson G, Spiegelman M, Weinstein M. 2010b. A multiscale model of partial melts: 2. Numerical results. *J. Geophys. Res.* 115(B4):B04411

Sinton J, Grönvold K, Sæmundsson K. 2005. Postglacial eruptive history of the western volcanic zone, Iceland. *Geochem. Geophys. Geosyst.* 6:Q12009

Sleep NH. 1984. Tapping of magmas from ubiquitous mantle heterogeneities: an alternative to mantle plumes? *J. Geophys. Res.* 89(B12):10029–41

Sleep NH. 1988. Tapping of melt by veins and dikes. *J. Geophys. Res.* 93(B9):10255–72

Spiegelman M. 2003. Linear analysis of melt band formation by simple shear. *Geochem. Geophys. Geosyst.* 4:8615

Spiegelman M, Elliott T. 1993. Consequences of melt transport for uranium series disequilibrium in young lavas. *Earth Planet. Sci. Lett.* 118:1–20

Spiegelman M, Kelemen P. 2003. Extreme chemical variability as a consequence of channelized melt transport. *Geochem. Geophys. Geosyst.* 4:1055

Spiegelman M, Kelemen P, Aharonov E. 2001. Causes and consequences of flow organization during melt transport: the reaction infiltration instability in compactible media. *J. Geophys. Res.* 106(B2):2061–77

Šrámek O, Ricard Y, Bercovici D. 2007. Simultaneous melting and compaction in deformable two-phase media. *Geophys. J. Int.* 168:964–82

Stevenson DJ. 1989. Spontaneous small-scale melt segregation in partial melts undergoing deformation. *Geophys. Res. Lett.* 16:1067–70

Stevenson DJ, Scott DR. 1991. Mechanics of fluid-rock systems. *Annu. Rev. Fluid Mech.* 23:305–39

Stracke A. 2021. A process-oriented approach to mantle geochemistry. *Chem. Geol.* 579:120350

Stracke A, Bourdon B, McKenzie D. 2006. Melt extraction in the Earth's mantle: constraints from U–Th–Pa–Ra studies in oceanic basalts. *Earth Planet. Sci. Lett.* 244:97–112

Takei Y. 2005. Deformation-induced grain boundary wetting and its effects on the acoustic and rheological properties of partially molten rock analogue. *J. Geophys. Res.* 110(B12):B12203

Takei Y. 2017. Effects of partial melting on seismic velocity and attenuation: a new insight from experiments. *Annu. Rev. Earth Planet. Sci.* 45:447–70

Takei Y, Holtzman B. 2009a. Viscous constitutive relations of solid-liquid composites in terms of grain boundary contiguity: 1. Grain boundary diffusion control model. *J. Geophys. Res.* 114(B6):B06205

Takei Y, Holtzman B. 2009b. Viscous constitutive relations of solid-liquid composites in terms of grain boundary contiguity: 2. Compositional model for small melt fractions. *J. Geophys. Res.* 114(B6):B06206

Takei Y, Holtzman B. 2009c. Viscous constitutive relations of solid-liquid composites in terms of grain boundary contiguity: 3. Causes and consequences of viscous anisotropy. *J. Geophys. Res.* 114(B6):B06207

Takei Y, Katz RF. 2015. Consequences of viscous anisotropy in a deforming, two-phase aggregate. Why is porosity-band angle lowered by viscous anisotropy? *J. Fluid Mech.* 784:199–224

Tirone M, Sessing J. 2017. Petrological geodynamics of mantle melting I. AlphaMELTS + multiphase flow: dynamic equilibrium melting, method and results. *Front. Earth Sci.* 5:81

Tolstoy M. 2015. Mid-ocean ridge eruptions as a climate valve. *Geophys. Res. Lett.* 42(5):1346–51

Turner S, Bourdon B. 2011. Melt transport from the mantle to the crust–uranium-series isotopes. In *Timescales of Magmatic Processes: From Core to Atmosphere*, ed. A Dosseto, SP Turner, JA Van Orman, pp. 102–15. Chichester, UK: Wiley-Blackwell

Turner S, Evans P, Hawkesworth C. 2001. Ultrafast source-to-surface movement of melt at island arcs from ^{226}Ra-^{230}Th systematics. *Science* 292:1363–66

Turner S, Reagan M, Vigier N, Bourdon B. 2012. Origins of ^{210}Pb-^{226}Ra disequilibria in basalts: new insights from the 1978 Asal Rift eruption. *Geochem. Geophys. Geosyst.* 13:Q07002

Tweed LEL. 2021. *Coupling the thermodynamics, kinetics and geodynamics of multiphase reactive transport in Earth's interior*. PhD Thesis, Columbia Univ., New York

Van Orman JA, Saal AE, Bourdon B, Hauri EH. 2006. Diffusive fractionation of U-series radionuclides during mantle melting and shallow-level melt–cumulate interaction. *Geochim. Cosmochim. Acta* 70:4797–812

von Bargen N, Waff HS. 1986. Permeabilities, interfacial areas and curvatures of partially molten systems: results of numerical computations of equilibrium microstructures. *J. Geophys. Res.* 91(B9):9261–76

Wang S, Constable S, Rychert CA, Harmon N. 2020. A lithosphere-asthenosphere boundary and partial melt estimated using marine magnetotelluric data at the central Middle Atlantic Ridge. *Geochem. Geophys. Geosyst.* 21:e2020GC009177

Wark DA, Watson E. 1998. Grain-scale permeabilities of texturally equilibrated, monomineralic rocks. *Earth Planet. Sci. Lett.* 164:591–605

Weatherley SM, Katz RF. 2012. Melting and channelized magmatic flow in chemically heterogeneous, upwelling mantle. *Geochem. Geophys. Geosyst.* 13:Q0AC18

White LT, Rawlinson N, Lister GS, Waldhauser F, Hejrani B, et al. 2019. Earth's deepest earthquake swarms track fluid ascent beneath nascent arc volcanoes. *Earth Planet. Sci. Lett.* 521:25–36

Wilson CR, Spiegelman M, van Keken PE, Hacker BR. 2014. Fluid flow in subduction zones: the role of solid rheology and compaction pressure. *Earth Planet. Sci. Lett.* 401:261–74

Yamauchi H, Takei Y. 2016. Polycrystal anelasticity at near-solidus temperatures. *J. Geophys. Res. Solid Earth* 121:7790–820

Yarushina VM, Podladchikov YY. 2015. (De)compaction of porous viscoelastoplastic media: model formulation. *J. Geophys. Res. Solid Earth* 120:4146–70

Yarushina VM, Podladchikov YY, Connolly JAD. 2015. (De)compaction of porous viscoelastoplastic media: solitary porosity waves. *J. Geophys. Res. Solid Earth* 120:4843–62

Yarushina VM, Podladchikov YY, Wang LH. 2020. Model for (de)compaction and porosity waves in porous rocks under shear stresses. *J. Geophys. Res. Solid Earth* 125:e2020JB019683

Zhang N, Behn MD, Parmentier EM, Kincaid C. 2020. Melt segregation and depletion during ascent of buoyant diapirs in subduction zones. *J. Geophys. Res. Solid Earth* 125:e2019JB018203

Zhu W, Hirth G. 2003. A network model for permeability in partially molten rocks. *Earth Planet. Sci. Lett.* 212:407–16

Annual Review
of Earth and
Planetary Sciences
Volume 50, 2022

Contents

Errata

An online log of corrections to *Annual Review of Earth and Planetary Sciences* articles may be found at http://www.annualreviews.org/errata/earth